PHYSICAL REVIEW A **107**, 052409 (2023)

Suppressing amplitude damping in trapped ions: Discrete weak measurements for a nonunitary probabilistic noise filter

Andrea Rodriguez-Blanco,[1,*] K. Birgitta Whaley,[2,3] and Alejandro Bermudez[4]
[1]*Departamento de Física Teorica, Universidad Complutense, 28040 Madrid, Spain*
[2]*Department of Chemistry, University of California, Berkeley, California 94720, USA*
[3]*Berkeley Center for Quantum Information and Computation, Berkeley, California 94720, USA*
[4]*Instituto de Física Teórica, UAM-CSIC, Universidad Autónoma de Madrid, Cantoblanco, 28049 Madrid, Spain*

(Received 18 September 2022; accepted 11 April 2023; published 16 May 2023)

The idea of exploiting maximally entangled states as a resource lies at the core of several modalities of quantum information processing, including secure quantum communication, quantum computation, and quantum sensing. However, due to imperfections during or after the entangling gates used to prepare such states, the amount of entanglement decreases and their quality as a resource gets degraded. We introduce a low-overhead protocol to reverse this degradation by partially filtering out a specific type of noise relevant to many quantum technologies. We present two trapped-ion schemes for the implementation of a nonunitary probabilistic filter against amplitude damping noise, which can protect any maximally entangled pair from spontaneous photon scattering during or after the two-qubit trapped-ion entangling gates. This filter can be understood as a protocol for single-copy quasidistillation, as it uses only local operations to realize a reversal operation that can be understood in terms of weak measurements.

DOI: 10.1103/PhysRevA.107.052409

I. INTRODUCTION

Entanglement allows for new ways of processing and transmitting information in the quantum-mechanical realm, including quantum teleportation as a paradigmatic example [1]. Given the important role of entanglement in diverse quantum-information protocols [2], it has become a genuine resource. For instance, maximally entangled states can be used for secure quantum communications [3–6], and for quantum sensing and metrology [7–9], both of which aim at beating the limitations imposed by the laws of classical physics. In the context of quantum computing, maximally entangled states between pairs of qubits in a quantum register can be prepared using gates drawn from a universal gate set. Improving the quality of these gates above a so-called fault-tolerance threshold is crucial to scale up these quantum computers [2,10–12]. Unfortunately, the quality of these entangled states, or the gates that produce them, gets degraded by small imperfections in the experimental controls as well as by the unavoidable coupling of the system to its surrounding environment. Therefore, a central goal across many quantum technologies is the development of techniques to create, store, and distribute maximally entangled states in the presence of decoherence and noise.

Amplitude damping is an important mechanism of decoherence arising from energy relaxation [2] that is common to many platforms. An example relevant to the present work is that of trapped-ion optical qubits [13–16], where spontaneous emission of photons from a metastable level leads to amplitude damping. This is summarized by the T_1 time, which sets the ultimate decoherence limit for optical qubits when all other sources of technical noise are suppressed. For trapped-ion hyperfine or Zeeman qubits [17,18], where the information is encoded in the ground state manifold, spontaneous photon scattering during storage vanishes. However, such photon scattering becomes relevant when creating and manipulating the entangled states, e.g., when using two-photon Raman transitions via auxiliary excited states, during which a residual emission of photons can contribute unfavorably to the gate fidelities [19,20]. Spontaneous emission can also be a limitation in Rydberg-atom quantum processors, where in order to achieve high two-qubit gate fidelities, long coherent ground-Rydberg state Rabi oscillations are needed. However, the presence of spontaneous emission decay channels from the intermediate excitation state to the ground manifold, and from the target Rydberg state to lower-n Rydberg states, with n the principal quantum number, limit the coherence and population times [21–23].

To fight against amplitude damping or, indeed any source of decoherence, one may redundantly encode the quantum-information into logical qubit by using more physical qubits. The theory of quantum error correction (QEC) shows that it is possible to exploit multipartite entanglement among the encoded physical qubits to actively detect and correct the errors that have occurred on the logical qubits without actually perturbing the encoded information [2,24–26]. In recent years, we have witnessed a remarkable progress in experimental QEC, especially in trapped-ion and superconducting-circuit platforms. We have seen how one logical qubit can be protected from an arbitrary error using 7 physical qubits for the color QEC code [27–29], or 9 [30,31], and 25 physical qubits

---

[*] andrer22@ucm.es

[32] for the surface QEC code. Moreover, the advantage of using fault-tolerant designs has also been demonstrated in Ref. [29,33]. This has allowed, for the first time, to realize a full universal gate set at the logical level, including transversal gates that create a logical entangled state using 14 physical qubits [29,33]. QEC strategies are known to provide a scalable solution to build large fault-tolerant quantum computers [34–36] that starts to become practically relevant as the experimental technologies increase the possible qubit redundancy. However, to achieve a significant advantage of quantum encoding when the noise and control errors lie in the vicinity of the aforementioned fault-tolerance threshold, even the most promising schemes of quantum error correction (QEC) [25,26,37] typically require a very high degree of redundancy which leads to large overheads in the number of physical qubits [35]. Thus there is still a long road ahead for truly large-scale QEC. In the meantime, it is important to develop alternative schemes that reduce the effect of noise with a lower qubit overhead. Moreover, some of these noise mitigation techniques could be eventually combined with QEC.

Some of these alternative strategies work best for specific types of noise. For instance, dynamical decoupling [38] refocuses the effects of dephasing noise caused by external fields with sufficiently slow fluctuations, whereas decoherence-free subspaces [39] exploit symmetric subspaces that are immune to external fields with sufficiently global fluctuations. In the context of QEC, the qubit overhead can also be reduced if one focuses on a set of errors that is believed to be the main noise source in a specific platform. Thus, one may devise channel-adapted QEC codes for amplitude damping by using four qubits to correct for one error [40,41]. In this work, we explore a different error suppression strategy that is framed in the context of *entanglement distillation* [42], which includes schemes for entanglement concentration and entanglement purification as specific limits, and will allow us to further minimize the qubit overhead. Such schemes are particularly relevant when the entanglement is distributed between a pair of spatially separated physical qubits.

For bipartite systems under realistic gates and channels, the prepared maximally entangled pairs are neither perfectly transformed under quantum operations nor perfectly distributed to distant parties. Entanglement distillation aims at exploiting local operations and classical communication (LOCC) to improve the fidelity of a collection of noisy partially entangled mixed states with respect to a target maximally entangled pure state [43]. We note that this question is not only of practical relevance in some applications, e.g., quantum repeaters for quantum communications over large distances [44], but has also played a key role in the development of the current understanding of entanglement via resource theories. Specifically, in a theoretical framework one considers extracting $m(n)$ maximally entangled pairs $|\Psi_{\rm AB}\rangle$ from n copies of a partially entangled mixed state $\rho_{\rm AB}$, by using a suitable LOCC protocol $\mathcal{E}\in$ LOCC. The efficiency of the distillation protocol is specified by the asymptotic ratio $m(n)/n\to\xi_{\rm D}$ in the limit of an infinite number of copies $n\to\infty$. This allows us to define the so-called distillable entanglement $E_{\rm D}(\rho_{\rm AB})=\sup_{\mathcal{E}\in{\rm LOCC}}\{\xi_D\}$, which corresponds to the optimal efficiency for all conceivable distillation protocols. This yields an operational measure of entanglement [45,46], quantifying the amount of entanglement in a state by the efficacy with which one can perform a particular task, namely, to distill perfect maximally entangled pairs from it.

From this theoretical perspective, distillation protocols aim at producing maximally entangled pairs with unit fidelity in such an asymptotic limit. In a seminal work [43], Bennett *et al.* showed that collective measurements on the qubits belonging to each of the parties separately, allow for a LOCC scheme that can distill a nonvanishing number of maximally entangled pairs from $n\to\infty$ copies, provided that the initial fidelity of the noisy mixed state is above $1/2$. It was then shown that this constraint on the initial state can be lifted, provided that one has previously applied a filtering operation to each of the separate copies [47]. This raised the question of exploring the capabilities of single-copy distillation schemes, which would thus reduce the large overhead in the number of partially entangled copies. To our knowledge, the first such scheme finds its root in the work on entanglement concentration for pure states by filtering [48], the so-called *Procrustean* method, which also applies to certain partially entangled mixed states [49]. We note that this single-copy distillation scheme has been realized in photonic experiments [50], where one aims at achieving the highest-possible fidelities by postselecting on the experimental outcomes of a generalized measurement [51]. In this context, the aforementioned theoretical limit of a perfect distilled state is unreachable, as the postselection probability drops to zero. In any case, since the filtering operations are always noisy in a practical experiment, the limit of perfect distillation is an idealization even for multicopy distillation schemes.

The link between quantum error suppression and entanglement distillation derives from the fact that single-copy distillation methods fall in the class of probabilistic quantum error detection (pQED) [52]. After the measurement, one can infer whether an error, e.g., amplitude-damping, has occurred or not, and then keep those outcomes where the encoded information can be probabilistically recovered by simply reversing the effect of the measurement [52,53]. The first proof-of-principle demonstrations of such pQED was performed in photonic systems using projective measurements implemented via photon absorption [50,54–56]. As remarked in Ref. [57], this absorptive measurement destroys the quantum state, such that the distilled entanglement cannot be used for any subsequent quantum-information task. In contrast, the trapped-ion experiment of Ref. [57] allowed demonstration of a two-copy distillation protocol that improves the quality of a single entangled pair which is not destroyed and thus remains available for further posterior processing. In a subsequent trapped-ion experiment [58], a shelving mechanism using additional states of the trapped-ion level structure was exploited to detect leakage without disturbing the qubit computational states. In the current work, we are interested in designing single-copy distillation schemes to fight against amplitude damping and protect any maximally entangled Bell pair created using trapped-ion technologies.

Although generic mixed states are not useful for perfect distillation [59,60], there are certain families of them that can be distilled arbitrarily close to the limit of unit fidelities [61]. This so-called *quasidistillation* is closer in spirit to the experimental situation, where the filtering operations are never perfect. As shown in Ref. [62], one can find optimal single-copy quasidistillation protocols with specific filtering operations that correspond to generalized measurements and depend on the form of the initial mixed state. These optimal strategies thus require prior information about the initial state, a property that is shared with the original Procrustean methods [48,49] and subsequent works [50,63,64]. In this work, we are interested in single-copy quasidistillation schemes where the filtering requires a priori information that is independent of the maximally entangled state one wants to distill. We show that this is possible for specific noise channels, where the prior information now depends on the noise. We present a low-resource probabilistic method to protect an unknown entangled pair against amplitude damping, which acts as a noise filter and is related to the Procrustean method of entanglement concentration [48]. The scheme presented here exploits a specific form of measurement reversal with origins in the context of weak measurements [65,66]. In addition to the focus on explicit mitigation of errors due to amplitude damping rather than on entanglement concentration in general, a technical difference from Ref. [48] is that the present scheme does not require any prior knowledge of the target state, which can be any of the maximally entangled states, but instead requires as an input parameter the T_1 time associated with the amplitude-damping noise. This can be determined from previous calibration experiments [13,14], and then fed into the probability of amplitude damping p for each qubit [67], namely

$$p = 1 - e^{-\frac{t}{T_1}}. \tag{1}$$

We provide two possible schemes for a trapped-ion implementation of this quasidistillation protocol. The first one is related to the idea of quantum logic spectroscopy [68] and exploits unitaries between the qubits and some of the common vibrational modes of the ion crystal holding them. The second method, on the other hand, exploits phonon-mediated entangling gates [69–71] to map the relevant information from the physical qubits onto the ancillas. The latter approach turns out to be more robust with respect to thermal fluctuations in the common vibrational modes. As noted above, this method can protect any unknown entangled pair, or even be applied at the level of the full entangling unitary that prepares such entangled pairs. Both methods exploit a measurement in which the physical qubit effectively interacts with an ancilla qubit, such that the ancilla gets flipped when an amplitude-damping error occurs, and can be used to design an operation that reverses the amplitude damping. The probabilistic character arises from the fact that we keep (postselect) those states for which the ancilla measurement signals “no error.” The method can thus also be viewed as acting as an amplitude-damping noise filter.

The remainder of the article is organized as follows: In Sec. II A, we present the general scheme to show how the filtering protocol based on quantum measurement reversals for amplitude damping can be used to distill single-copy entangled states. In Sec. III we then propose two different schemes for the experimental implementation of the quantum measurement reversals in trapped-ion platforms. Adapted to the trapped-ion native logic operations, the first method in Sec. III A relies on quantum logic spectroscopy techniques mediated by common vibrational modes. The second method in Sec. III B consists on a sequence of one and two-qubit gates, both of which are quite robust to the thermal motion of the ions. Finally, in Sec. IV, we benchmark both schemes while highlighting the power to protect any entangled state by calculating the average gate fidelity and discuss their practical limitations under more realistic conditions. Section V summarizes and presents an outlook for further development.

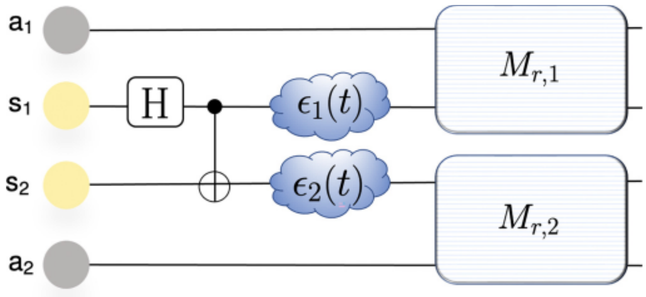

FIG. 1. Amplitude-damping reversal for single-copy distillation. We consider a pair of physical or system qubits s_1, s_2, which can be prepared in a maximally entangled Bell pair (2) via a Hadamard gate H and an entangling CNOT gate, as shown in the circuit. The system qubits are then subjected to uncorrelated amplitude damping channels, Eq. (3), which may model the main error source during the gate or the primary source of environmental noise during a waiting period t. The resulting partially entangled mixed state can be distilled into a state with a higher fidelity with respect to the targeted Bell pair via the reversal operations $M_{r,1}$, $M_{r,2}$, Eq. (6), which act as nonunitary filters and must be implemented by coupling the qubits to ancillary degrees of freedom a_1, a_2, and postselecting on specific outcomes of subsequent measurements.

II. NOISE FILTERING AGAINST AMPLITUDE DAMPING

A. General scheme

Consider a pair of qubits s_1, s_2 that can be prepared in any Bell pair by a maximally entangling unitary $U_{\rm id}$. Using the first two unitary gates of the circuit displayed in Fig. 1 with $U_{\rm id} = U_{\rm CNOT}$, we have

$$U_{\rm id}|\pm\rangle_{s_1}\otimes|0\rangle_{s_2} = |\Phi_\pm\rangle = \tfrac{1}{\sqrt{2}}\big(|0\rangle_{s_1}\otimes|0\rangle_{s_2} \pm |1\rangle_{s_1}\otimes|1\rangle_{s_2}\big),$$
$$U_{\rm id}|\pm\rangle_{s_1}\otimes|1\rangle_{s_2} = |\Psi_\pm\rangle = \tfrac{1}{\sqrt{2}}\big(|0\rangle_{s_1}\otimes|1\rangle_{s_2} \pm |1\rangle_{s_1}\otimes|0\rangle_{s_2}\big). \tag{2}$$

As outlined in the introduction, we aim at designing a probabilistic filtering method that, in contrast to previous entanglement concentration schemes [43,57] can protect any of these maximally entangled states and requires prior information about the noise instead of the particular state. We note that this entangling operation might be any other unitary gate native to the specific experimental setup. In fact, the scheme can also be applied to quantum network scenarios where entanglement between distant qubits is heralded via photonic interconnects, as has been demonstrated for trapped ions [72–78]. In that case, the scheme below serves to quasidistill a specific target entangled pair from the heralded two-qubit state.

Our scheme thus serves to protect the full entangling unitary $\rho_{\rm id}=U_{\rm id}\rho_0U_{\rm id}^\dagger$ against an amplitude damping channel

$$\rho_{\rm id}\mapsto\tilde{\rho}_{\rm id}=\epsilon(\rho_{\rm id})=\epsilon_{\rm s_1}\circ\epsilon_{\rm s_2}(\rho_{\rm id}),\tag{3}$$

which is represented by the shaded clouds in Fig. 1. Here we have defined

$$\epsilon_{\rm s_q}(\rho_{\rm id})=K_{0,\rm s_q}\rho_{\rm id}K_{0,\rm s_q}^\dagger+K_{1,\rm s_q}\rho_{\rm id}K_{1,\rm s_q}^\dagger,\tag{4}$$

in terms of the Kraus operators $K_{0,\rm s_1}=K_0\otimes\mathbb{I}_2$, $K_{0,\rm s_2}=\mathbb{I}_2\otimes K_0$, $K_{1,\rm s_1}=K_1\otimes\mathbb{I}_2$, $K_{1,\rm s_2}=\mathbb{I}_2\otimes K_1$, with

$$K_0=\begin{pmatrix}1&0\\0&\sqrt{\bar{p}}\end{pmatrix},\quad K_1=\begin{pmatrix}0&\sqrt{p}\\0&0\end{pmatrix},\tag{5}$$

where p is the probability of an amplitude damping error and $\bar{p}=1-p$ is the probability that no amplitude-damping error occurs, with p dependent on the T_1 time via Eq. (1). These single-qubit Kraus operators defined in the computational basis represent the amplitude damping noise channel [2,41]. This is an asymmetric channel since the qubit states $|1\rangle_{\rm s_q}$ are transformed to $|0\rangle_{\rm s_q}$ with probability $0<p\leqslant 1$, while the $|0\rangle_{\rm s_q}$ states never transform into $|1\rangle_{\rm s_q}$, regardless of the value of p. As noted above, the amplitude-damping probability can be related to the natural lifetime of the qubit, due, e.g., to photon scattering from a metastable level in trapped-ion optical qubits, or to the residual photon-scattering when the entangling gate is mediated by two-photon processes via far-detuned dipole-allowed transitions.

If the decoherence due to amplitude damping is caused by photon emission into the electromagnetic (EM) environment, we can effectively understand the decay channel as a partial (often referred to as a weak) measurement of the photon number exerted by the aforementioned environment [67]. The partial collapse of the amplitudes from the excited to the ground state can then be seen as the result of weak measurements performed by the independent EM modes that can absorb the emitted photon by each of the system qubits. In contrast to the more common von Neumann projections [2], a weak measurement does not fully collapse the quantum state into an eigenstate of the operator being measured, and is thus reversible [52,79,80]. Therefore, for decay probabilities $0<p<1$, a secondary weak measurement can be applied to reverse the partial collapse, leading to a quantum measurement reversal of the aforementioned errors [80].

This reversal can be accomplished by a filtering operation. In the case of amplitude damping, this corresponds to the last pair of operations depicted in Fig. 1, which read

$$\begin{aligned}\tilde{\rho}_{\rm id}&\mapsto M_{r,2}M_{r,1}\tilde{\rho}_{\rm id}M_{r,1}M_{r,2},\\ M_{r,q}&=\frac{1}{\sqrt{P_{r_q}}}\begin{pmatrix}\sqrt{\bar{p}_{r_q}}&0\\0&1\end{pmatrix}.\end{aligned}\tag{6}$$

Note that these reversal operations are applied to each of the physical qubits forming the partially entangled pair. As discussed in detail below, to implement such a nonunitary filter, the physical qubits must be coupled to an ancillary subsystems, which must then be measured. In Eq. (6), P_{r_q} is the postselection success probability. We note that the fidelity of the recovery process will never be strictly equal to one, as it is a nontrace-preserving map [52,65].

Let us illustrate how the filtering method works for a particular entangled state. Consider the circuit shown in Fig. 1 with the system qubits initialized in the tensor product state $|1\rangle_{\rm s_1}\otimes|1\rangle_{\rm s_2}$ such that the Hadamard gate on the first qubit and the unitary $U_{\rm id}=U_{\rm CNOT}$ create the pure maximally entangled state $\rho_{\rm id}=U_{\rm id}\rho_0U_{\rm id}^\dagger=|\Psi_-\rangle\langle\Psi_-|$. The system qubits can undergo amplitude damping either during the gate, or after a subsequent memory time t. Assuming that both qubits are identical and subjected to the same uncorrelated noise environments, the decay probabilities can be considered to be the same, $p_1=p_2=p$, and the density matrix evolves to the partially mixed entangled-state

$$\rho_{\rm id}\mapsto\tilde{\rho}_{\rm id}=p|0,0\rangle\langle 0,0|+\bar{p}\rho_{\rm id}.\tag{7}$$

Recalling that $\bar{p}=1-p$, we see that with probability p the amplitudes of the excited states on the entangled pair decay to the two-qubit tensor product ground state $|0,0\rangle=|0\rangle_{\rm s_1}\otimes|0\rangle_{\rm s_2}$, while with probability $1-p$, the system remains in the pure maximally entangled state. The unfiltered state infidelity in this situation is equal to p, i.e.,

$$\varepsilon_{\rm unf}=1-\mathcal{F}_{\rm unf}=1-\langle\Psi_-|\tilde{\rho}_{\rm id}|\Psi_-\rangle=p.\tag{8}$$

We now use the amplitude damping filtering protocol to distill a single-copy and increase the fidelity with the target entangled state. As emphasized above, our scheme is independent of the initial maximally entangled state and it is also valid for any entangling gate, in particular for the Mølmer-Sørensen (MS) gates of trapped ion architectures that we will use later on. The reason for this generality is that the protocol focuses on removing the additional amplitude that decayed from the excited states to the ground states. The amount that needs to be removed is proportional to the decay probability of Eq. (1) and thus it is only the specific value of T_1 that is required as prior information to implement the single-copy distillation. The decay removal procedure is carried out by applying a quantum measurement reversal on each qubit, with equal strengths $p_{r_1}=p_{r_2}=p_r$, such that the density matrix transforms according to Eq. (6). This leads to

$$\tilde{\rho}_{\rm id}\mapsto\rho_{\rm f}=\frac{1}{P_r}\left(\bar{p}_r^2p|00\rangle\langle 00|+\bar{p}_r\bar{p}\rho_{\rm id}\right),\tag{9}$$

where $P_r=\bar{p}_r^2p+\bar{p}_r\bar{p}$ is a normalization constant that represents the success probability of the measurement reversal. The probability of decaying to the common ground state is now $\bar{p}_r^2p/P_r$, and the probability of remaining in the maximally entangled state is now $\bar{p}_rp/P_r$. By setting the strength of the reversal operation equal to the probability of amplitude decay [Eq. (1)], namely, $p_r=p$, we get

$$\rho_{\rm f}=\frac{1}{\bar{p}^2(p+1)}(\bar{p}^2p|00\rangle\langle 00|+\bar{p}^2\rho_{\rm id}).\tag{10}$$

We see that the probability of decaying to the ground state has now been effectively reduced by a factor of $1/(1+p)$. This increases the filtered fidelity by the same factor, so that

$$\varepsilon_{\rm f}=1-\mathcal{F}_{\rm f}=\frac{p}{1+p}.\tag{11}$$

This example illustrates how the filtering protocol can be used for single-copy quasidistillation. The distillation power increases with increasing p, i.e., with increasing time t, since the infidelity ratio $\varepsilon_{\mathrm{f}}/\varepsilon_{\mathrm{unf}} = 1/(1+p)$ decreases with p. However, the probability of successful filtering, P_r, also decays with time according to its dependence on p [see below Eq. (10)]. For instance, after two different combinations of gate or memory times, such as $t/T_1 = 1/10$ and $t/T_1 = 1$ with associated decay probabilities of $p(1/10) = 0.01$ and $p(1) = 0.63$, the corresponding probabilities of quasidistillation success will be $P_r \approx 0.90$ and $P_r \approx 0.20$, respectively. This clearly shows how the probabilistic nature of the method arises, as well as the trade-off between a higher quality distillation and a more frequent distillation. For a number of repetitions $N = 100$, we will be filtering out part of the amplitude damping correctly in 90 instances for the first case, while for the second case, the correct instances reduce to 20. Consequently, for a given number N of experimental runs, the greater the amplitude decay probability p, the fewer the successful events where the noise is suppressed.

Having presented and illustrated the scheme in this section, the remaining task is to describe how one can implement such filtering operations in practical setups. In the context of weak measurements, employing a quantum measurement reversal to reverse the effect of noise can be realized by first applying a weak measurement and then applying the reversal operation. This idea has been previously addressed both theoretically and experimentally for single qubits, in solid-state systems [65], superconducting qubits [81–83], trapped ions [58,84] and photonic systems [85,86]. However, the reversal of a partial collapse on entangled states has only been considered for photonic systems [66,85,87–89]. In the next section we develop a filtering scheme based on weak quantum measurement reversal for single-copy distillation of any entangled state for trapped-ion platforms. We point out that the procedure described here also provides protection against amplitude damping for single trapped-ion qubits. In fact, the quantum measurement reversal operation in Eq. (6) is defined as the tensor product of a quantum measurement reversal on each of the qubits. Therefore, the two measurement reversal schemes presented in this work can be readily adjusted to fight against amplitude damping in single qubits by substituting one of the quantum measurement reversals by the identity operator. Our primary interest here, however, focuses on single-copy distillation of any entangled state for trapped-ions and on increasing the fidelity of the full two-qubit entangling unitary. In current trapped-ion implementations, two-qubit gates are the major bottleneck to perform quantum error correction codes near pseudothresholds or to achieve a high-fidelity logical state preparation. The low qubit overhead of our scheme makes it interesting as an alternative to standard QEC, since it can effectively suppress the effect of noise on platforms and/or applications which at present are only capable of manipulating a relatively small number of qubits. Moreover, it is also practical for communication situations, where the physical qubits are held by distant parties, and conventional QEC is not straightforward.

The full protocol to implement this nonunitary filter is based on the construction of asymmetric positive operator-valued measure (POVM) operators followed by postselection on ancilla qubits. Section III introduces two different schemes to perform the necessary asymmetric POVMs. The first scheme builds on the work presented in Ref. [84], where a theoretical formalism to implement symmetric POVMs for trapped ions using quantum logic spectroscopy (QLS) operations [68] was discussed. Here, we extend this QLS scheme to the design of asymmetric POVM operators, which will be crucial to exploit them as nonunitary filters for single-copy distillation against amplitude damping. The main difference between symmetric and asymmetric POVMs is that, while in the symmetric case one always recovers the projectors onto computational basis for the extremal cases with $p_r = 0$ and $p_r = 1$, in the asymmetric case one recovers either the identity r a single projection operator in these limits, but never two projectors.

As discussed in detail in Sec. III A, this QLS scheme exploits common vibrational modes between the system and ancillary qubits, which should be previously laser cooled to the vibrational ground state. This makes nonunitary filtering susceptible to thermal fluctuations in the common vibrational mode, compromising in this way the efficacy of the distillation method. We present a detailed account of this error source below. In Sec. III B we then present the second scheme that is not ultimately restricted to the ions operating in the vacuum vibrational mode. Similarly inspired by the case of symmetric POVMs [84], we show that now the asymmetric reversal of amplitude damping can be implemented in terms of single and two-qubit gates [90], which are far more robust to the specific motional state of the ions. As discussed in detail below, these gates must be followed by projective measurement and postselection on the ancilla qubits. In Sec. IV we compile the resulting circuits into native trapped-ion gates and compare the average gate fidelities of a two-qubit gate in the presence and absence of the filtering process.

III. IMPLEMENTATION OF QUANTUM MEASUREMENT REVERSAL FOR TRAPPED IONS

In this section, we give a detailed account of the two schemes for implementation of asymmetric POVMs in trapped ion architectures and discuss how these connect to the nonunitary filters of Eq. (6) for single-copy quasidistillation. Common to both schemes is the need to use one ancilla qubit per system qubit in order to perform the probabilistic error detection. Thus, for the two-qubit maximally entangled state, two ancilla qubits must be added to the qubit register. We now discuss how the common vibrational modes, togther with projective measurements on the ancillas, can be exploited to perform the desired POVM.

A. Scheme A: Asymmetric positive operator-valued measures via quantum logic spectroscopy

The scheme to realize an asymmetric POVM consists of a series of unitary operations applied to the system and ancilla ions, followed by a final projective measurement on the ancilla qubits that postselects certain outcomes. The underlying idea is similar to that of quantum logic spectroscopy (QLS) [68], in which information stored in the system qubits can be coherently transferred onto the ancilla ions through the

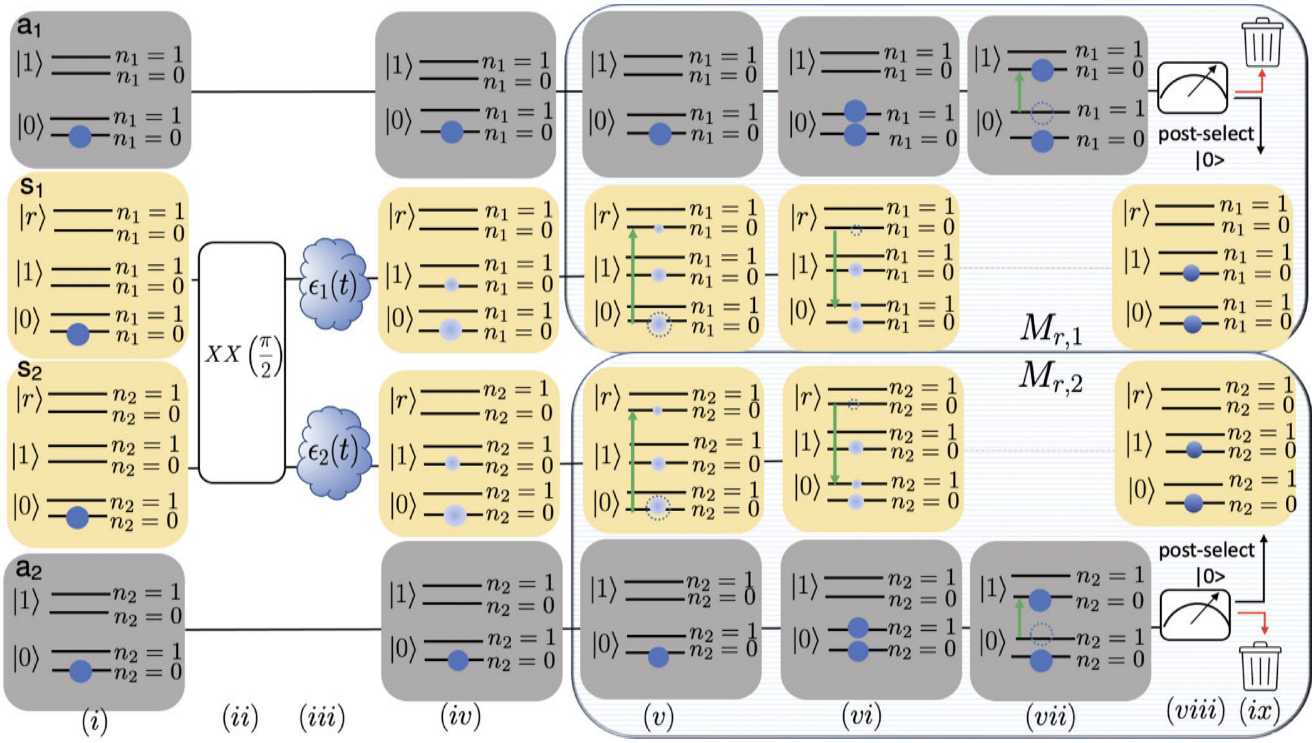

FIG. 2. Amplitude-damping reversal by quantum logic spectroscopy. The system s_1, s_2 and ancillary a_1, a_2 subsystems of Fig. 1 are composed of both internal and motional levels. In the left-hand side, we include the two lowest Fock states for the vibrational ladder of states associated with each of the system and ancilla qubits. Note that the vibrational Fock levels of s_1, a_1 (and of s_2, a_2) correspond to the same common mode. (*i*) The initial state has no internal or motional excitation. Using the trapped-ion native gates, (*ii*) an entangled pair is generated by the entangling gate $XX(\pi/2)$ (12), which is followed by (*iii*) the amplitude-damping channels $\epsilon_1(t)$, $\epsilon_2(t)$ (4), depicted by two clouds, that act during a time t that sets the error rate (1). The resulting effect, summarized in (*iv*), is to shuffle the amplitudes, as depicted by the dashed blue circles of the subsequent column. The reversal or filtering operations that are then carried out to distill a better entangled state and reverse the environmental noise are depicted inside the following two boxes, which correspond to the sequence of carrier (*v*) and sideband pulses [*vi* and *vii*], followed by (*viii*) a projective measurement, and (*ix*) postselection on the ancillas. As discussed in the text, by adjusting the duration of the pulses (14), and postselecting on the measurement outcomes (20), one obtains the desired nonunitary filter (6).

common vibrational modes provided by the Coulomb interaction between the ions. The procedure ends with a projective measurement of the ancilla qubits that induces a POVM on the system qubits. The optimal implementation would use ancilla ions from a different atomic species or isotope, which reduces the effect that light scattering during a fluorescence-enabled measurement of the ancillas can have on the system qubits. Alternatively, ion shuttling could be used to transport the ancilla ions to a measurement trapping region located far away from the system qubits [91,92]. We note that another possibility to implement an asymmetric POVM without ancillas is to use more internal states of the ions, as discussed in Refs. [58,93].

The initial stage of construction of our asymmetric POVMs proceeds by analogy to the symmetric case [84] and thus exploits three different levels from the atomic level structure of the ions. We denote these by $\{|0\rangle_{\mathrm{s_q}}, |1\rangle_{\mathrm{s_q}}, |r\rangle_{\mathrm{s_q}}\}$ for the ions $\mathrm{q} = \{1, 2\}$ that store the two system or data qubits (see Fig. 1). The state $|r\rangle_{\mathrm{s_q}}$ is an auxiliary metastable excited state that connects the qubits states in a lambda configuration. The two ancillary subsystems a_1, a_2 also shown in Fig. 1 are provided by additional ions, each of which contributes with a pair of internal levels, which are initially prepared in the state $\rho_{\mathrm{a}}(t_0) = |0\rangle\langle 0|_{\mathrm{a}_1} \otimes |0\rangle\langle 0|_{\mathrm{a}_2}$. The system and ancilla ions form a linear chain aligned along the null of the rf-field of a Paul trap that confines the ion register. Accordingly, their Coulomb interaction couples the small vibrations around the ion crystal equilibrium position, giving rise to the common vibrational modes. We select two specific vibrational modes, m_1 and m_2, each of which describes specific collective vibrations along a particular axis direction k_1 and k_2. Assuming initial laser-cooling conditions to the ground state of both modes, the motional state can be described by the tensor product of two Fock states with no vibrational quanta, $\rho_{\mathrm{m}}(t_0) = |0\rangle\langle 0|_{\mathrm{m}_1} \otimes |0\rangle\langle 0|_{\mathrm{m}_2}$. The initial state of the scheme is then written as the tensor product state $\rho(t_0) = \rho_{\mathrm{s}}(t_0) \otimes \rho_{\mathrm{a}}(t_0) \otimes \rho_{\mathrm{m}}(t_0)$, where $\rho_{\mathrm{s}}(t_0)$ represents the internal state of the system qubits that, after being subjected to the entangling gate depicted in Fig. 2, is close to one of the four maximally entangled pairs, i.e., the four Bell states.

We assume that the remaining vibrational modes do not intervene in the protocol and thus act as mere spectators. We also assume that the heating on each of the vibrational modes is vanishingly small. Using a trapped-ion native gate set, we can remove the Hadamard gate in Fig. 1 by using a Mølmer-Sørensen (MS) gate [94,95] instead of the CNOT gate, specified by

$$U_{\rm id} = XX\left(\frac{\pi}{2}\right) = \frac{1}{\sqrt{2}}\left(\mathbb{I} - i\sigma^x_{\rm s_1}\sigma^x_{\rm s_2}\right). \tag{12}$$

This entangling gate, represented by $XX(\pi/2)$ in Fig. 2, readily generates four maximally entangled pairs on the system qubits that are locally equivalent to the Bell states of Eq. (2). In the left-hand side of this figure, step (i) represents an initial state with the system and ancilla qubits initialized in $|0\rangle$. Note that we also draw the two lowest vibrational Fock levels for the corresponding common modes, which will be used in subsequent steps. In step (ii), the MS gate produces the entangled pair $(|0\rangle_{\rm s_1}\otimes|0\rangle_{\rm s_2} - i|1\rangle_{\rm s_1}\otimes|1\rangle_{\rm s_2})/\sqrt{2}$ for the system qubits. In step (iii), this unitary is followed by the amplitude decay channel described by Eq. (3), leading to a partially entangled mixed state $\rho_{\rm id} = U_{\rm id}\rho(t_0)U^\dagger_{\rm id} \mapsto \tilde{\rho}_{\rm id}$. As a consequence of spontaneous emission, the probabilities to find the system qubits in either of the two possible states will now no longer be equal, which is depicted in step (iv) by the different size of the shaded blue balls of the corresponding levels.

We now show how to construct an asymmetric POVM that can reverse the amplitude damping. This requires a sequence of gates to implement $M_{r,q}$ in Eq. (6), which is depicted inside the two rectangular boxes on the right of Fig. 2. The scheme starts with three consecutive unitary operations, steps (v)–(vii). The first one, step (v), is $O_1 = R^c_{\rm s_1}(\theta_1,\phi_1)\otimes R^c_{\rm s_2}(\theta_1,\phi_1)$, and consists of a carrier pulse on each system ion in resonance with the transition $|0\rangle_{\rm s_q}\to|r\rangle_{\rm s_q}$ [96]. This reads

$$R^{\rm c}_{\rm s_q}(\theta_1,\phi_1) = \exp\left\{i\frac{\theta_1}{2}\left(e^{i\phi_1}\sigma^+_{\rm s_q} + e^{-i\phi_1}\sigma^-_{\rm s_q}\right)\right\}, \tag{13}$$

where $\sigma^+_{\rm s_q} = |r\rangle\langle 1|_{\rm s_q}$ $(\sigma^-_{\rm s_q} = |1\rangle\langle r|_{\rm s_q})$ are the spin raising (lowering) operators. This carrier pulse, represented by the green arrows of the first carrier pulse in the boxes of Fig. 2, must act for a specific duration

$$t_1 = \frac{2}{\Omega^c_1}\cos^{-1}(\sqrt{1-p_r}). \tag{14}$$

We set $\phi_1 = 0$ in Eq. (13), and define the pulse area $\theta_1 = \Omega^c_1 t_1$ in terms of the carrier Rabi frequency Ω^c_1, which depends on a parameter p_r that controls the strength of the reversal operation. In Fig. 2, the effect of this carrier is depicted by a partial transfer of the shaded blue amplitude to the auxiliary r level.

In step (vi) we then apply a red-sideband pulse $O_2 = R^{\rm rsb}_{\rm s_1,m_1}(\theta_2,\phi_2)\otimes R^{\rm rsb}_{\rm s_2,m_2}(\theta_2,\phi_2)$ to each of the system ions [96]. This corresponds to the unitary

$$R^{\rm rsb}_{\rm s_q,m_q}(\theta_2,\phi_2) = \exp\left\{i\frac{\theta_2}{2}\left(e^{i\phi_2}\sigma^+_{\rm s_q}a_{\rm m_q} + e^{-i\phi_2}\sigma^-_{\rm s_q}a^\dagger_{\rm m_q}\right)\right\}, \tag{15}$$

where $a_{\rm m_q}$ $(a^\dagger_{\rm m_q})$ are the annihilation (creation) operators of phonons in the common vibrational mode $\rm m_q$. This sideband is resonant with the transition $|r\rangle_{\rm s_q}\otimes|n\rangle_{\rm m_q}\to|0\rangle\otimes_{\rm s_q}|n+1\rangle_{\rm m_q}$, which increases the phonon number of the corresponding vibrational Fock state. To map the relevant information into the common mode, we set the phase to $\phi_2 = 0$, and the pulse area to $\theta_2 = \pi$, such that the pulse duration is

$$t_2 = \frac{\pi}{\Omega^{\rm rsb}_2}. \tag{16}$$

Here, we use the definition of the red-sideband Rabi frequency $\Omega^{\rm rsb}_2 = \eta\Omega^c_2$, where Ω^c_2 is the carrier Rabi frequency of this second pulse, $\eta = (\hbar k_L/2M_{\rm m}\omega_{\rm m_q})^{1/2}$ is the Lamb-Dicke parameter defined in terms of the frequency of the mth vibrational mode $\omega_{\rm m_q}$, and the mass of the ions $M_{\rm m}$ determines the contribution of the ion q to the specific normal mode.

In Fig. 2, the effect of this sideband pulse is depicted by green lines pointing down, which partially transfer the shaded blue amplitude of the r level onto the vibrational Fock state.

At this stage, we make use of the ancillary qubits by mapping the amplitude of the common vibrational Fock state onto the internal states of the ancilla qubits. For the third operation in step (vii), $O_3 = R^{\rm rsb}_{\rm a_1,m_1}(\theta_3,\phi_3)\otimes R^{\rm rsb}_{\rm a_2,m_2}(\theta_3,\phi_3)$, we thus apply another red-sideband pulse to each ancilla qubit

$$R^{\rm rsb}_{\rm a_q,m_q}(\theta_3,\phi_3) = \exp\left\{i\frac{\theta_3}{2}\left(e^{i\phi_3}\sigma^+_{\rm a_q}a_{\rm m_q} + e^{-i\phi_3}\sigma^-_{\rm a_q}a^\dagger_{\rm m_q}\right)\right\}. \tag{17}$$

In this case, the sideband is in resonance with the transition $|0\rangle_{\rm a_q}|n+1\rangle_{\rm m_q}\to|1\rangle_{\rm a_q}|n\rangle_{\rm m_q}$, and we set the phase and pulse area to $\phi_3 = 0$ and $\theta_3 = \pi$, respectively. Accordingly, the time duration is again

$$t_3 = \frac{\pi}{\Omega^{\rm rsb}_3}, \tag{18}$$

where all parameters are defined by analogy with the previous red-sideband pulse.

Following the scheme of Fig. 2, this operation acts on the ancillary subspaces depicted by gray circles inside the two boxes, where the green lines point upwards and denote how the vibrational Fock excitation is converted into an excitation of the ancilla qubits.

The final step $(viii)$, which is crucial to engineering the POVM and the nonunitary filter, consists of a projective measurement on each of the ancilla qubits. This is followed by postselecting in step (ix) on the outcomes that are consistent with the state $|0\rangle_{\rm a_q}$. Using the projectors

$$E^{\sigma_{\rm a_q}}_{\pm} = \left(\mathbb{I}\pm\sigma^z_{\rm a_q}\right)/2, \tag{19}$$

where $\sigma^z_{\rm a_q} = |0\rangle\langle 0|_{\rm a_q} - |1\rangle\langle 1|_{\rm a_q}$ for $\rm q = \{1,2\}$, the reduced density matrix for the system is equivalent to a POVM measurement with the four possible outcomes

$$\tilde{\rho}_{\rm id}\to\begin{cases} M_{r,2}M_{r,1}\tilde{\rho}_{\rm id}M_{r,1}M_{r,2}, \text{ if ancillas in } |0\rangle_{\rm a_1}\otimes|0\rangle_{\rm a_2},\\ \overline{M}_{r,2}M_{r,1}\tilde{\rho}_{\rm id}M_{r,1}\overline{M}_{r,2}, \text{ if ancillas in } |0\rangle_{\rm a_1}\otimes|1\rangle_{\rm a_2},\\ M_{r,2}\overline{M}_{r,1}\tilde{\rho}_{\rm id}\overline{M}_{r,1}M_{r,2}, \text{ if ancillas in } |1\rangle_{\rm a_1}\otimes|0\rangle_{\rm a_2},\\ \overline{M}_{r,2}\overline{M}_{r,1}\tilde{\rho}_{\rm id}\overline{M}_{r,1}\overline{M}_{r,2}, \text{ if ancillas in } |1\rangle_{\rm a_1}\otimes|1\rangle_{\rm a_2}.\end{cases} \tag{20}$$

Here, we have introduced the following operators $M_{r,1} = M_r\otimes\mathbb{I}$, $M_{r,2} = \mathbb{I}\otimes M_r$, and similarly for $\overline{M}_{r,1}$, $\overline{M}_{r,2}$, where

$$M_r = \frac{1}{\sqrt{P_r}}\begin{pmatrix}\sqrt{\bar{p}_r} & 0\\ 0 & 1\end{pmatrix},\quad \overline{M}_r = \frac{1}{\sqrt{\overline{P}_r}}\begin{pmatrix}\sqrt{p_r} & 0\\ 0 & 1\end{pmatrix}, \tag{21}$$

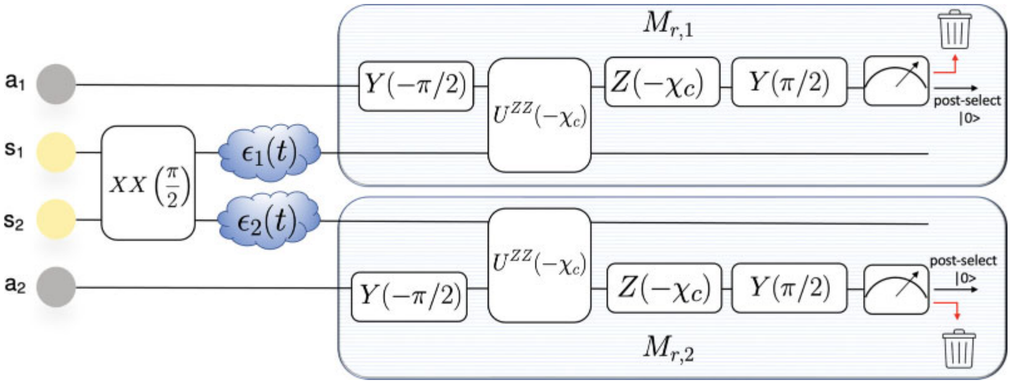

FIG. 3. Amplitude-damping reversal by system-ancilla entangling gates. In this scheme, the two blocks that realize the reversal operations $M_{r,1}$, $M_{r,2}$ are modified from those in Fig. 2. Here, we perform a sequence of rotations on the ancilla qubits $Y(\pm\pi/2)=e^{\pm i\pi\sigma^y_{\rm a_q}/4}$, and $Z(\pm\pi/2)=e^{i\chi_{\rm c}\sigma^z_{\rm a_q}/2}$, together with an entangling geometric phase gate $U^{ZZ}(-\chi_{\rm c})=e^{i\chi_{\rm c}\sigma^z_{\rm a_q}\sigma^z_{\rm s_q}}$. The specific ordering is depicted in the two shaded boxes, which also include the ancilla projective measurement and postselection.

and the probability for the outcomes is determined by $P_r=\text{Tr}\{M^\dagger_{r,i}M_{r,i}\rho_{\rm s}\}$, with $\overline{P}_r=1-P_r$. These POVMs resemble the Kraus operators for the asymmetric amplitude damping channel of Eq. (5) are also manifestly asymmetric, since in the limit $p_r\to 1$, the POVM operator M_r maps onto a von Neumann projection, $M_r\to|1\rangle\langle 1|$, which connects the reversal operations with an infinitely sharp, i.e., a strong projective measurement onto a single qubit state, while for $p_r\to 0$ the POVM operator M_r maps to the identity matrix, which has no effect on the qubit states. These POVMs thus represent an asymmetric version of a weak measurement, in contrast to the symmetric POVMs proposed for QLS in Ref. [84].

It is now a straightforward to see how this asymmetric POVM can be used to reverse the asymmetric amplitude-damping channel. By postselecting on those measurement outcomes consistent with the $|0\rangle_{\rm a_q}$ state, we are effectively applying the projection $O_4=E_+^{\sigma_{\rm a_1}}E_+^{\sigma_{\rm a_2}}$, and thereby introducing the nonunitary character of the filtering process. The output density matrix after all these consecutive steps reads

$$\rho_{\rm f}=M_{r,2}M_{r,1}\tilde{\rho}_{\rm id}M_{r,1}M_{r,2}, \tag{22}$$

in accordance with Eq. (6). Note that the reversal parameter p_r can be fully controlled by modifying the timing of the first carrier pulse (14). If we look at the effect of the original amplitude-damping channel with Kraus operators (5), it is clear that the reversal operator M_r in Eq. (21) can invert most of the effect of the amplitude damping if one controls the time duration of the carrier pulse such that

$$p_r=p=1-e^{-t/T_1}. \tag{23}$$

Essentially, the nonunitary filter reduces the amplitude of the $|0\rangle_{\rm s_q}$ system qubit states to increase the fidelity with the target entangled state, leading to a single-copy probabilistic quasidistillation. The practical observation is that the prior information required for this quasidistillation is no longer related to the amplitudes of the initial entangled state, as in the Procrustean method [48,49], but instead depends on the T_1 time of the noise channel (23) and can serve to protect any maximally entangled pair. Let us also emphasize that each of the blocks of Fig. 2, which lead to the corresponding filters $M_{r,1}$ and $M_{r,2}$ are only composed of LOCC operations. The two partially entangled qubits $\rm s_1$, $\rm s_2$ can thus be spatially separated, and these LOCC operators serve to distill a state with a larger fidelity with the target maximally entangled state, as will be discussed with specific numerical simulations in the following section.

B. Scheme B: Asymmetric positive operator-valued measures via entangling gates

In this section, we introduce a different scheme that still requires using two ancilla qubits, but no longer relies on motional Fock states with a single motional excitation. Instead, it exploits two-qubit gates between system and ancilla qubits, which are mediated by off-resonant excitations of the common motional modes in a way that is considerably insensitive to the thermal populations [96]. The scheme is summarized in Fig. 3. The full unitary part of the scheme can be described by the following operator

$$U_{\rm q}=e^{i\frac{\pi}{4}\sigma^y_{\rm a_q}}e^{i\frac{\chi_c}{2}\sigma^z_{\rm a_q}}e^{i\frac{\chi_c}{2}\sigma^z_{\rm a_q}\sigma^z_{\rm s_q}}e^{-i\frac{\pi}{4}\sigma^y_{\rm a_q}}, \tag{24}$$

which must be applied to each separate pair $\rm s_q$, $\rm a_q$ for $\rm q=\{1,2\}$. This unitary combines single-qubit rotations on the ancilla qubits with an entangling geometric phase gate [90] between the ancilla and the corresponding system qubit. We have found that in order to implement the asymmetric POVMs (6), the geometric phase of the later must be

$$\chi_c=\cos^{-1}(\sqrt{1-p_r}), \tag{25}$$

which is the analog of Eq. (14) in the previous QLS-based scheme.

Following these operations, as depicted in Fig. 3, the final step consists of a projective measurement and postselection on the ancilla qubit in state $|0\rangle_{\rm a_q}$ as in the previous scheme. Finally, the output density matrix after these four consecutive steps can be written as

$$\rho_{\rm f}=M_{r,2}M_{r,1}\tilde{\rho}_{\rm id}M_{r,1}M_{r,2}, \tag{26}$$

where we have introduced $M_{r,\mathrm{q}} = E_{+}^{\sigma_{\mathrm{aq}}} U_{\mathrm{q}}/\sqrt{P_r}$ in terms of the previous ancilla projectors $E_{+}^{\sigma_{\mathrm{aq}}}$, with the corresponding postselection probabilities $P_r = \mathrm{Tr}\{M_{r,\mathrm{q}}^{\dagger} M_{r,\mathrm{q}} \tilde{\rho}_{\mathrm{id}}\}$.

In the following section, we will show numerically that this scheme also implements the desired nonunitary filter, and that it is more robust than the scheme of Sec. III A to thermal fluctuations of the vibrational mode that is used to mediate the geometric phase gate.

IV. RESULTS

So far, we have presented the single-copy quasidistillation protocol and discussed two possible schemes to realize the protocol in trapped-ion platforms. We have also illustrated how it can improve the fidelity of a specific mixed state resulting from amplitude-damping noise (11). As remarked already, an interesting property of the filtering scheme is that it can work for any target entangled state. To show that this is indeed the case, in this section, we present analytical and numerical results showing that both schemes lead to the desired single-copy quasidistillation, and also address some possible practical limitations. The criterion to determine the success of the nonunitary probabilistic filtering to protect any entangled state against amplitude damping is dictated by the increase of the average gate fidelity of the noisy implementation of the unitary U_{id}.

In Sec. IV A we now present analytical formulas when the whole filtering protocol is executed under ideal conditions and numerical results validating the performance of the protocol as a tool for suppression of errors due to amplitude damping. In Secs. IV B and IV C we then show numerical results for more realistic situations that could limit the performance of the protocol for each scheme.

A. Ideal implementation of the filtering schemes

To compare an ideal unitary operation with its actual implementation due to noise and experimental imperfections, we use the measure provided by the average gate fidelity [2], namely,

$$\bar{\mathcal{F}}_g(U_{\mathrm{id}}, \epsilon) = \int d\Psi_0 \langle \Psi_0 | U_{\mathrm{id}}^{\dagger} \epsilon(\tilde{\rho}_{\mathrm{id}}) U_{\mathrm{id}} | \Psi_0 \rangle. \tag{27}$$

Here U_{id} is the target unitary and $\epsilon(\tilde{\rho}_{\mathrm{id}})$ represents the evolution of the system under imperfect implementations of the unitary. Complete preservation of the quantum information implies $\bar{\mathcal{F}}_g(U_{\mathrm{id}}, \epsilon) = 1$, which corresponds to a perfect implementation of the unitary with $\epsilon = \mathbb{I}$, i.e., zero noise.

The integral in Eq. (27) must be performed over the Hilbert space of all possible initial two-qubit states Ψ_0. Alternatively, one can estimate $\bar{\mathcal{F}}_g(U_{\mathrm{id}}, \epsilon)$ by the entanglement fidelity [51,61,97], which is defined for a single initial state $|\phi_m\rangle$ that is a maximally entangled state of the system with an auxiliary quantum system, according to

$$\bar{\mathcal{F}}_e(U_{\mathrm{id}}, \epsilon) = \langle \phi_m | \mathbb{I}_d \otimes U_{\mathrm{id}}^{\dagger} \epsilon(|\phi_m\rangle\langle\phi_m|) \mathbb{I}_d \otimes U_{\mathrm{id}} | \phi_m \rangle. \tag{28}$$

Here U_{id} is an N qubit (or qudit) unitary acting on the system alone. This measure makes use of an initial state $|\phi_m\rangle = \sum_{\alpha=1}^{d} |\alpha\rangle \otimes |\alpha\rangle/\sqrt{d}$ that is maximally entangled between two subsystems. In our case these are first the $N = 2$ data qubits where the information is encoded, and second an auxiliary system with two spectator qubits. The dimension of the N-qubit unitary is then $d = 2^N = 4$. Both the unitary $\mathbb{I}_d \otimes U_{\mathrm{id}}$, and the noise channel $\epsilon(|\phi_m\rangle\langle\phi_m|) = \mathbb{I}_d \otimes \epsilon(\tilde{\rho}_{\mathrm{id}})$, only act on the data qubits while the spectator qubits remain unaffected.

Remarkably, one can derive a simple formula connecting the entanglement fidelity with the gate fidelity [51,61], namely,

$$\bar{\mathcal{F}}_{\mathrm{g}}(U_{\mathrm{id}}, \epsilon) = \frac{d\bar{\mathcal{F}}_e(U_{\mathrm{id}}, \epsilon) + 1}{d + 1}. \tag{29}$$

Since, $\bar{\mathcal{F}}_g \geqslant \bar{\mathcal{F}}_e$ [97], the entanglement fidelity represents a lower bound for the average gate fidelity.

We now derive analytical expressions for the entanglement fidelity of our protocol in both the absence and presence of the noise-filtering operations. The unitary gate we consider is the two-qubit entangling gate $U_{\mathrm{id}} = XX(\frac{\pi}{2})$, Eq. (12), and the noise evolution $\epsilon(\tilde{\rho}_{\mathrm{id}})$ is given in terms of the Kraus operators for the uncorrelated noise channels of Eqs. (3) and (4). We choose $|\alpha\rangle \in \{|00\rangle, |01\rangle, |10\rangle, |11\rangle\}$ for the set of operator basis states. Starting from Eq. (28), the entanglement fidelity for the unfiltered evolution reduces to

$$\bar{\mathcal{F}}_e^{\mathrm{unf}}(U_{\mathrm{id}}, \epsilon) = \frac{1}{4d^2} \left| \sum_{i,j=0}^{1} \mathrm{Tr}\left\{K_{i,\mathrm{s}_1} \otimes K_{j,\mathrm{s}_2}\right\} \right|^2, \tag{30}$$

with $d = 4$ for $N = 2$ system qubits, where we have made use of the analysis in Ref. [98] to write the result in terms of the Kraus operators.

Including the reversal and filtering operations to distill a single-copy entangled state, and applying $M_r = M_{r,1} \otimes M_{r,2}$ in Eq. (6) via either scheme A (Sec. III A) or scheme B (Sec. III B), modifies the entanglement fidelity to

$$\bar{\mathcal{F}}_e^{\mathrm{f}}(U_{\mathrm{id}}, \epsilon) = \frac{1}{4d^2 P_r} \left| \sum_{i,j=0}^{1} \mathrm{Tr}\left\{M_r\left(K_{i,\mathrm{s}_1} \otimes K_{j,\mathrm{s}_2}\right)\right\} \right|^2. \tag{31}$$

Here P_r is the probability of success of the reversing operation, given by $P_r = \mathrm{Tr}\{M_r^{\dagger} M_r \epsilon(|\phi_m\rangle\langle\phi_m|)\}$.

The implementation of M_r and hence the sequence of gates employed for the realization of the protocol differs between the QLS-based and entangling-based schemes presented in Sec. III. In scheme A (Fig. 2), M_r takes the form

$$M_r^A = M_{r,1}^A \otimes M_{r,2}^A = O_4 O_3 O_2 O_1, \tag{32}$$

where the various operations O_i correspond to the set of unitaries depicted inside the box of Fig. 2, applied to each of the two parties. In particular, we use the carrier pulses $O_1 = R_{\mathrm{s}_1}^{c}(\theta_1, \phi_1) \otimes R_{\mathrm{s}_2}^{c}(\theta_1, \phi_1)$ in Eq. (13), the sidebands $O_2 = R_{\mathrm{s}_1,\mathrm{m}_1}^{\mathrm{rsb}}(\theta_2, \phi_2) \otimes R_{\mathrm{s}_2,\mathrm{m}_2}^{\mathrm{rsb}}(\theta_2, \phi_2)$ in Eq. (15), and $O_3 = R_{\mathrm{a}_1,\mathrm{m}_1}^{\mathrm{rsb}}(\theta_3, \phi_3) \otimes R_{\mathrm{a}_2,\mathrm{m}_2}^{\mathrm{rsb}}(\theta_3, \phi_3)$ in Eq. (17). Finally, $O_4 = E_{+}^{\sigma_{\mathrm{a}_1}} E_{+}^{\sigma_{\mathrm{a}_2}}$ are the projectors $E_{\pm}^{\sigma_{\mathrm{aq}}} = (\mathbb{I} \pm \sigma_{\mathrm{a}_\mathrm{q}}^{z})/2$ onto the $|0\rangle_{\mathrm{a}_\mathrm{q}}$ states for both ancilla qubits a_1 and a_2, that are used for postselection.

For scheme B (Fig. 3), the reversal operation is instead implemented by the sequence of unitaries

$$M_r^B = M_{r,1}^B \otimes M_{r,2}^B = U_1 \otimes U_2, \tag{33}$$

where U_1 and U_2 are described by the sequence of single and two-qubit gates given in Eq. (24), which involve the ancilla-system qubit pairs, $\{\mathrm{a}_1, \mathrm{s}_1\}$ and $\{\mathrm{a}_2, \mathrm{s}_2\}$, respectively.

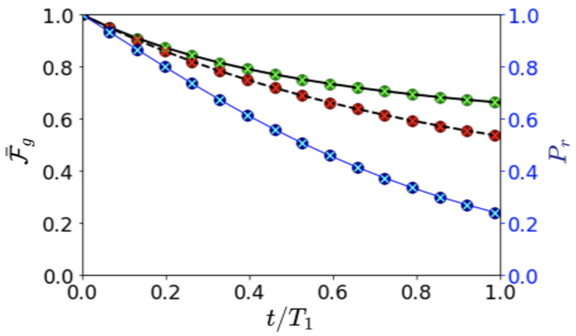

FIG. 4. Average gate fidelities and success probability for ideal case implementation of error reversal schemes A and B. Plotted lines correspond to the analytical formulas from Sec. IV A as specified below. Solid circles and cross symbols represent the results of the numerical simulations of the process following scheme A and scheme B, respectively. The black font y axis on the left represents the filtered average gate fidelity and the blue y axis on the right represents the success probability P_r. The x axis represents time in units of the amplitude damping decay time T_1. $T_1 = 0.8$ s for the results shown here. The black (upper) solid line is the expression for the analytical average gate fidelity $\bar{\mathcal{F}}_g^{\rm f}$ (35) when the filtering protocol is implemented after the unitary. Scattered green dots (lime crosses) on top of the upper line represent the numerical simulations of the average gate fidelities for scheme A (B), $\bar{\mathcal{F}}_g^{\rm f,A}$ ($\bar{\mathcal{F}}_g^{\rm f,B}$). The dashed black (middle) line is the unfiltered average gate fidelity $\bar{\mathcal{F}}_g^{\rm unf}$ (34). Scattered maroon dots (red crosses) on top of the middle line are the simulations of the unfiltered average gate fidelity for scheme A (B), $\bar{\mathcal{F}}_g^{\rm unf,A}$ ($\bar{\mathcal{F}}_g^{\rm unf,B}$). The blue (bottom) solid line is the success probability of the process given by $P_r = {\rm Tr}\{M_r^\dagger M_r \epsilon(|\phi_m\rangle\langle\phi_m|)\}$. Scattered blue dots (cyan crosses) on top of the bottom line are the simulations of the unfiltered average gate fidelity for scheme A (B), $P_{r,A}$ ($P_{r,B}$). The measurement reversal operation, M_r, takes the form of Eqs. (32) and (33), for schemes A and B, respectively.

For the ideal case scenario where the gates have no errors and one assumes an initial motional ground state, numerical simulation of the performance of both nonunitary filters against amplitude damping errors leads to the same result, namely $M^A_{r,j} = M^B_{r,j} = M_{r,j}$ in Eq. (6). This is confirmed by numerical simulations of the protocol of scheme A and scheme B using a full-density matrix formalism. Therefore, in the ideal case, both schemes yield the same entanglement fidelity, $\bar{\mathcal{F}}_e^{\rm f} = \bar{\mathcal{F}}_e^{\rm f,A} = \bar{\mathcal{F}}_e^{\rm f,B}$, as is also evident from Eq. (30). Using Eq. (29) then implies identical average gate fidelities, which is verified in the numerical results plotted in Fig. 4. However, we expect that in more realistic situations, e.g., when thermal fluctuations are present, this will not necessarily be the case. This will be investigated in Secs. IV B and IV C where we show the effect of nonzero vibrational excitation in the initial state, $\bar n > 0$, when implementing $M^A_{r,j}$ and $M^B_{r,j}$, respectively.

Before turning to such discussion of imperfections, we continue here with the ideal case, considering the special case of equal amplitude-decay probabilities on both ions, $p_1 = p_2 = p$. In this case we can find an analytical expression for the unfiltered average gate fidelity independently of the scheme, which is given by

$$\bar{\mathcal{F}}_g^{\rm unf} = \frac{1}{5}\left(1+\frac{(1+\sqrt{\bar p})^4}{4}\right), \tag{34}$$

and clearly depends only on the error probability. The analogous quantity for the filtered case with identical strength of the reversal operations on both ions set equal to the probability of decay, i.e., $p_r = p$ is given by

$$\bar{\mathcal{F}}_g^{\rm f} = \frac{1}{5}\left(1+\frac{16\bar p^2}{4P_r}\right) = \frac{1}{5}\left(1+\frac{16}{(2+p)^2}\right). \tag{35}$$

Here the expression for the success probability that appears in the denominator is $P_r = \bar p^2(2+p)^2/4$.

Figure 4 shows plots of the analytic expressions for gate fidelity in the ideal case, together with the corresponding numerical simulations as a function of the gate time, where this is measured in units of t/T_1. The dashed black (middle) line represents the analytic unfiltered average gate fidelity [Eq. (34)], while the black solid (upper) line is the analytical average gate fidelity when the filtering is applied. The fidelity under filtering always lies above the unfiltered case, and thus shows the benefits of the weak measurement reversal. The dot and cross markers represent the results for the numerical simulations according to scheme A (QSL-based) and scheme B (entangling based), respectively.

As mentioned in Sec. I, where we discussed an example of quasidistillation into the Bell pair $|\Psi_-\rangle$, the advantage of the proposed scheme is more significant at longer times. It is interesting to note that in the limit of large t, the unfiltered average gate fidelity drops below 1/2 and reaches the limit of $\bar{\mathcal{F}}_g^{\rm unf} = 0.25$, while the filtered gate fidelity never drops below the value $\bar{\mathcal{F}}_g^{\rm f} = 0.55$. Note that, for any biseparable state, the fidelity $F \leqslant 1/2$ whereas the fidelity is always greater than one-half, $F > 1/2$, for entangled states [99,100]. Thus, by applying the filtering operation, we can ensure that the system qubits remain in an entangled state. This can be easily characterized in current experiments using stabilizer-based witnesses [101–103] without the need to measure the full density matrix [2]. Despite these positive features, however, the probability does always decrease with time, as depicted by the blue solid (bottom) line in Fig. 4. So for large t, it is unlikely that one can reverse the amplitude decay and recover the maximally entangled states.

B. Limitation on scheme A: Warm vibrational modes

The QLS-based protocol, scheme A, was discussed above in the limit of zero occupation number for both vibrational modes. However, in current experimental architectures, one commonly has $\bar n > 0$ and the motional modes should then be described by the tensor product $\rho^{\rm th}_{\{\rm m_q\}} = \rho^{\rm th}_{\rm m_1} \otimes \rho^{\rm th}_{\rm m_2}$ of two Gibbs states of the form

$$\rho^{\rm th}_{\rm m_q} = \sum_{n_{\rm m_q}=0}^{\infty} p_{\rm m_q}(n_{\rm m_q})|n_{\rm m_q}\rangle\langle n_{\rm m_q}|, \tag{36}$$

where the probability $p_{\rm m_q}(n_{\rm m_q})$ is given by the thermal mode distribution

$$p_{\rm m_q}(n_{\rm m_q}) = \frac{1}{1+\bar n_{\rm m_q}}\left(\frac{\bar n_{\rm m_q}}{1+\bar n_{\rm m_q}}\right)^{n_{\rm m_q}}. \tag{37}$$

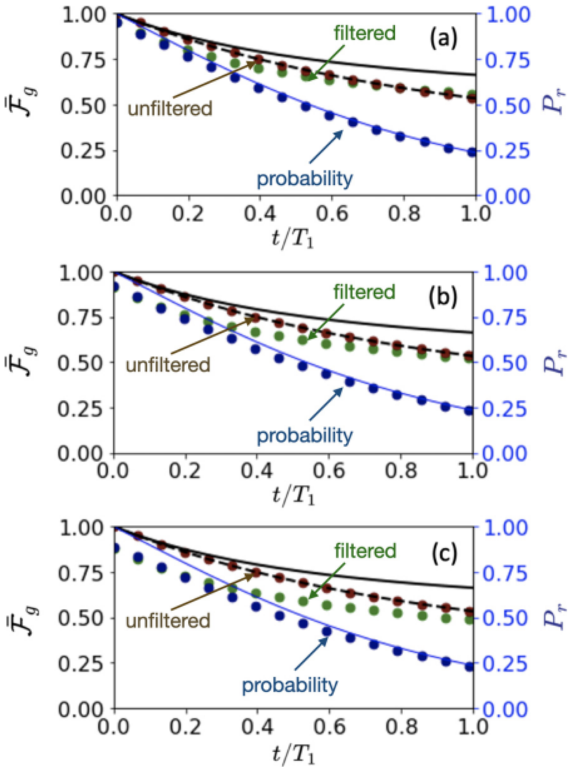

FIG. 5. Average gate fidelities and success probability for scheme A with $\bar{n} > 0$. Numerical simulations of scheme A for two motional modes with average phonon number $\bar{n}_{\rm m} = \bar{n}_{{\rm m}_1} = \bar{n}_{{\rm m}_2} > 0$. Instead of starting with two Fock states with $\bar{n} = 0$ as in the ideal case, we initialize the motional modes using two Gibbs states (36) with three different values of finite average phonon number: (a) $\bar{n}_{\rm m} = 0.05$, (b) $\bar{n}_{\rm m} = 0.09$, and (c) $\bar{n}_{\rm m} = 0.125$. The black font y axis on the left represents the average gate fidelity and the blue y axis on the right represents the success probability P_r. The x axis represents time in units of the amplitude damping time T_1. $T_1 = 0.8$ s for the results shown here. The black solid (top) lines represent the analytic and ideal-case average gate fidelities when the filtering protocol is implemented after the unitary, i.e., $\bar{\mathcal{F}}_g^{\rm f}$. The dashed black (middle) lines are the analytical and ideal-case unfiltered average gate unfiltered fidelities, and the blue solid (bottom) lines are the result of the success probabilities of the process simulated for different occupation numbers. The scattered green ("filtered"), maroon ("unfiltered"), and blue ("probability") dots represent the numerically simulated results under nonideal conditions for the filtered average gate fidelity $\bar{\mathcal{F}}_g^{\rm f}$, the unfiltered average gate fidelity $\bar{\mathcal{F}}_g^{\rm unf}$, and the success probability P_r, respectively.

Here $\bar{n}_{{\rm m}_{\rm q}} = 1/(e^{k_{\rm B}T_{{\rm m}_{\rm q}}/\hbar\omega_{{\rm m}_{\rm q}}} - 1)$ is the Bose-Einstein distribution, $\omega_{{\rm m}_{\rm q}}$ is the frequency of the $m_{\rm q}$ mode, and $T_{{\rm m}_{\rm q}}$ is an effective temperature for the mode. The resulting thermal fluctuations in the initial state will introduce errors in the system-ancilla mapping, and hence in the subsequent postselected measurements on the ancillas, leading to imperfect filtering. To characterize these deviations, we numerically simulate the same sequence of unitaries discussed for the ideal case, with the vacuum motional state replaced by the thermal state (36).

Figure 5 shows how both the fidelity after the probabilistic filtering, $\bar{\mathcal{F}}_g^{\rm f}$ (green dotted "filtered" line), and the success probability P_r (blue dotted "probability" line) decrease as the mean number of vibrational excitations $\bar{n}$ grows. Figures 5(a)–5(c), show the results obtained assuming that the two vibrational modes exploited for QLS of each system-ancilla ions have been sideband-cooled to the same temperature, with different mean numbers of phonons $\bar{n} = 0.05$, $\bar{n} = 0.09$, and $\bar{n} = 0.125$, respectively. Comparing with the results for the ideal case $\bar{n} = 0$ (black-solid lines), we see how the filtered average gate fidelity $\bar{\mathcal{F}}_g^{\rm f}$ (scattered green dots) degrades significantly for even a small increase in the initial vibrational excitation number $\bar{n}0$. It is interesting to note that, when the amplitude decay is not too large, with this imperfection the gate fidelity after noise filtering (green "filtered" dotted line) can actually be worse than for the unfiltered case (dashed black-lines and maroon "unfiltered" dots). This is visible already for $\bar{n} > 0.05$, where the filtering method is seen to provide no advantage for times $t/T_1 < 1/2$—here the unfiltered average gate fidelity (dashed black-lines and maroon "unfiltered" dots) lies above the filtered one. This effect becomes larger as the mean number of phonons $\bar{n}$ increases. For $\bar{n} > 0.125$, the filtering barely adds any advantage, and it even drops below $1/2$ when $t \to T_1$. The success probabilities (blue dotted "probability" line) also drop with increasing average phonon number, such that one would get a reduced number of postselected events. These results clearly show how sensitive the QLS-based scheme A is to thermal motion. For this reason it is imperative to have an alternative method such as the entanglement-based scheme B. In the next section we discuss the performance of scheme B in the presence of its most serious source of imperfections.

C. Limitation on entanglement based scheme B: Warm active and spectator modes along the trap axis

As already mentioned previously, scheme B does not rely on motional Fock states having a single motional excitation like scheme A. Instead, scheme B exploits the two-qubit gates $U^{ZZ}(-\chi_{\rm c}) = e^{i\chi_{\rm c}\sigma^z_{\rm aq}\sigma^z_{\rm sq}}$ between system and ancilla qubits, that is significantly less sensitive to the thermal populations. The $U^{ZZ}(-\chi_{\rm c})$ gates implemented in the scheme are robust with respect to thermal occupation of the active vibrational modes in the ideal scenario described in Sec. III B. This ideal scenario is the one in which the laser beams are perfectly aligned along one out of the three branches of phonons (one branch per trap symmetry axis $\alpha = x, y, z$). With N ions, we have N normal modes of oscillation per branch, each with an associated normal-mode frequency $\omega_{\alpha,m_{\rm q}}$ and $m_{\rm q} \in 1, \dots N$. We choose a particular axis of vibrational motion α, and mode $m_{\rm q}$ to implement the entangling gates. This is the active mode, while the rest of the $(N-1)$ modes on that axis are considered as spectator modes. In the ideal scenario, it is assumed that the residual qubit-phonon coupling with the modes that do not participate in the state-dependent force can be neglected. There are, however, corrections of a higher order in the Lamb-Dicke parameter, $\eta_{{\rm m}_{\rm q}}$, which are not far off-resonant and must be considered as a possible source of errors. Here, we study how such coupling of the warm active and spectator modes along the trap axis to the active entangling mode affect the performance of scheme B. The geometric phase χ_c of the entangling gates between ancilla and system qubits relates to the spin-spin coupling strength $J_{\mathrm{a_q,s_q}}$ and the gate time t_g according to $J_{\mathrm{a_q,s_q}}t_g = -\chi_c$, with [104]

$$U_{\mathrm{a_q,s_q}}(t_g) = e^{-iJ_{\mathrm{a_q,s_q}}t_g\sigma^z_{\mathrm{a_q}}\sigma^z_{\mathrm{s_q}}} = e^{i\chi_c\sigma^z_{\mathrm{a_q}}\sigma^z_{\mathrm{s_q}}}, \tag{38}$$

where $\chi_c = \cos^{-1}(\sqrt{1-p_r})$. In the presence of warm modes, the coupling strength takes the form

$$J_{\mathrm{a_q,s_q}} = -\sum_{m_q}^{N}\frac{2}{\delta_{\mathrm{m_q}}}\frac{|\tilde{\Omega}_{\mathrm{L,a_q}}||\tilde{\Omega}_{\mathrm{L,s_q}}|}{4}\eta^2_{\mathrm{m_q}}M_{\mathrm{a_q,m_q}}M_{\mathrm{s_q,m_q}} \times\left(1-\eta^2_{\mathrm{m_q}}a^\dagger_{\mathrm{m_q}}a_{\mathrm{m_q}}-\sum_{m'_q\neq m_q}\eta^2_{\mathrm{m'_q}}a^\dagger_{\mathrm{m'_q}}a_{\mathrm{m'_q}}\right)\cos(\phi^\circ_{\mathrm{a_q,s_q}}), \tag{39}$$

where $\tilde{\Omega}_{\mathrm{L,i}} = \Omega_{\mathrm{L}}e^{-\frac{1}{2}\sum_{\mathrm{m_q}}(\eta_{\mathrm{m_q}}\mathcal{M}_{\mathrm{i,m_q}})^2}$ includes the crossed-beam AC-Stark shifts of the transition Ω_{L}, multiplied by the Debye-Waller factor [105,106], which accounts for a renormalization due to the zero-point fluctuations of the ions. Here M_{i,m_q} are the normal-mode displacements of ion i along a given axis direction for the m_{q}th mode [107], $\delta_{\mathrm{m_q}}$ are the detunings of the laser frequency from the different mode frequencies, $a_{\mathrm{m_q}}$ ($a'_{\mathrm{m_q}}$) is the annihilation operator for the active (spectator) modes and $a^\dagger_{\mathrm{m_q}}$ ($a'^\dagger_{\mathrm{m_q}}$) are the annihilation operators of the active (spectator) phonons in the common vibrational mode $n_{\mathrm{m_q}}$, and $\eta_{\mathrm{m_q}}$ is the Lamb-Dicke parameter.

This analysis shows that thermal fluctuations on the vibrational modes will lead to deviations from the target condition $J_{\mathrm{a_q,s_q}}t_g = -\chi_c$. Equation (39) predicts the leading error due to thermal phonons on the active mode to be $\eta^2_{\mathrm{m_q}}a^\dagger_{\mathrm{m_q}}a_{\mathrm{m_q}}$ which is $O(\{\eta^2_{\mathrm{m_q}}\})$, and the leading error due to $N-1$ warm spectator modes along the same axis α to be $\sum_{m'_q\neq m_q}\eta^2_{\mathrm{m'_q}}a^\dagger_{\mathrm{m'_q}}a_{\mathrm{m'_q}}$ which is similarly $O(\{\eta^2_{\mathrm{m'_q}}\})$. These two corrections will add fluctuations to the phase of the entangling gate. However, the geometric phase closure conditions are not modified by thermal fluctuations. The form of the phase-space distribution may change, but the phase-space trajectory still closes after the same time $t_g = 2\pi r/\delta_{\mathrm{m_q}}$, where r is the number of loops in phase space. If we fix the laser intensities such that, after this time, the area acquired in phase space leads to the desired χ_c, we can estimate how scheme B gets affected by the average number of phonons using the relation

$$-J_{i,j}(\{\bar{n}_{\mathrm{m_q}}\})t_g = \chi_c = \cos^{-1}(\sqrt{1-p_r})O(\{\bar{n}_{\mathrm{m_q}}\}), \tag{40}$$

where the leading corrections $O(\{\bar{n}_{\mathrm{m_q}}\})$ due to warm phonons on the trap axis direction are given by

$$O(\{\bar{n}_{\mathrm{m_q}}\}) = 1-\eta^2_{\mathrm{m_1}}\left[\bar{n}_{\mathrm{m_1}}+\left(\frac{\omega_{\mathrm{m_1}}}{\omega_{\mathrm{m_2}}}\right)\bar{n}_{\mathrm{m_2}} +\left(\frac{\omega_{\mathrm{m_1}}}{\omega_{\mathrm{m_3}}}\right)\bar{n}_{\mathrm{m_3}}+\left(\frac{\omega_{\mathrm{m_1}}}{\omega_{\mathrm{m_4}}}\right)\bar{n}_{\mathrm{m_4}}\right]. \tag{41}$$

Here $\bar{n}_{\mathrm{m_q}}$ represent the average number of phonons on each mode. This expression is specific to the $N=4$ ion-chain depicted in Fig. 3. For a given axis α, we choose the active mode to be the center-of-mass (COM) mode and set the frequency of this as $\omega_{\mathrm{m_1}} = \omega_{\mathrm{COM}}$. According to Ref. [108], the frequencies for the remaining $N-1$ axial modes in an $N=4$ chain are $\omega_{\mathrm{m_2}} = \sqrt{3}\omega_{\mathrm{m_1}}$, $\omega_{\mathrm{m_3}} = \sqrt{5.81}\omega_{\mathrm{m_1}}$, and $\omega_{\mathrm{m_4}} = \sqrt{9.308}\omega_{\mathrm{m_1}}$. Figure 6 shows the result of a numerical simulation of the reversal operation $M_r = M_r^B$ using the strength from Eq. (40) for a linear chain with $N=4$ ions of the same species confined in a Paul trap having an axial COM frequency of $\omega_{\mathrm{COM}} = 2\pi\times 1.4$ MHz and a Lamb-Dicke parameter of $\eta_1\equiv\eta_{\mathrm{COM}} = 0.026$. In the presence of warm axial phonons the measurement reversal operation M_r^B in scheme B can be written in the general form as

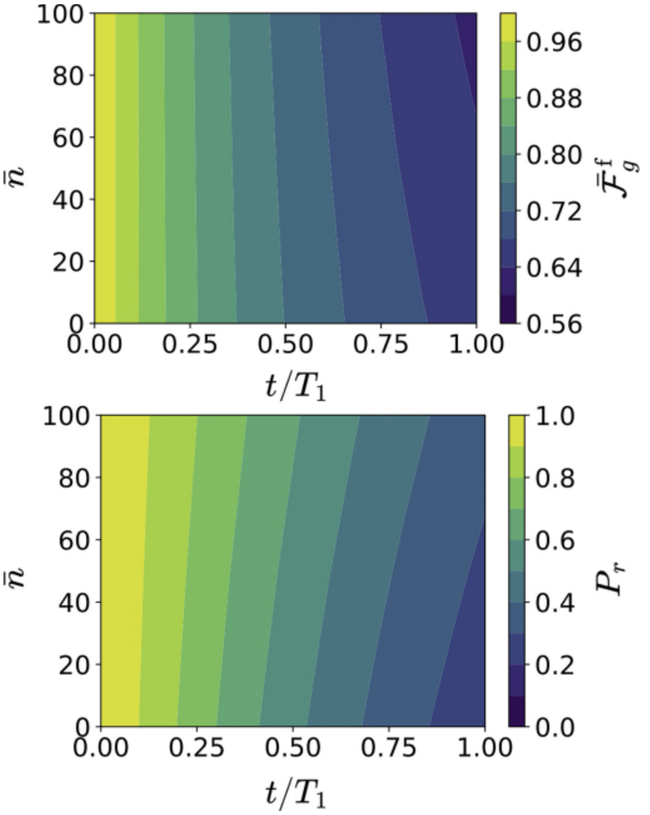

FIG. 6. Effect of warm active phonons along the trap axis for scheme B. Numerical results for simulation of scheme B following the sequence from Fig. (3) with $\chi_c = \cos^{-1}(\sqrt{1-p_r})O(\{\bar{n}\})$ as the strength of the measurement reversal, and $O(\{\bar{n}\})$ (41) the leading corrections due to the warm phonons. The y axes represent the average phonon number for each of the four modes which we set to be equal $\bar{n} = n_{\mathrm{m_1}} = n_{\mathrm{m_2}} = n_{\mathrm{m_3}} = n_{\mathrm{m_4}}$ while the x axis represents the time in units of the amplitude damping time T_1. For the results shown in here we considered $T_1 = 0.8$ s. The colormap sidebar on the top panel represent the filtered or distilled average gate fidelity for different $\bar{n}$ and t/T_1 units of time. The colormap on the bottom panel does the same but for the probability of success.

$$M_r^B = \frac{1}{\sqrt{P_r}}\begin{pmatrix}\cos^2(\chi_c) & 0 & 0 & 0\\ 0 & \cos(\chi_c) & 0 & 0\\ 0 & 0 & \cos(\chi_c) & 0\\ 0 & 0 & 0 & 1\end{pmatrix}, \tag{42}$$

where the geometric phase χ_c, Eq. (25), is now corrected by the term $O(\{\bar{n}_{\mathrm{m_q}}\})$ [see Eqs. (40) and (41)]. P_r is the probability of success of the reversing operation, which is given by

$$P_r = \tfrac{1}{4}[\cos^4(\chi_c)(p+1)^2 + 2\cos^2(\chi_c)\bar{p}(1+\bar{p}) + \bar{p}^2]. \quad (43)$$

In the case where all axial modes are in the ground state $\bar{n} = 0$, $O(\{\bar{n}_{\mathrm{m_q}}\}) = 1$, we recover the ideal case for which $\chi_c(t/T_1, \bar{n} = 0) = \cos^{-1}(\sqrt{1 - p_r})$ (25). For the limiting cases $t/T_1 = 0$ and $t/T_1 = 1$, the geometric phase takes the values $\chi_c(0, \bar{n} = 0) = 0$ and $\chi_c(1, \bar{n} = 0) = 1.005$, respectively, yielding $P_r(\chi_c = 0) = 1$ and $P_r(\chi_c = 1.005) = 0.151$. Hence, for a fixed value of $p_r = p$, the success probability P_r in Eq. (43), would be higher for smaller values of χ_c. Now, in the presence of warm phonons $\bar{n} > 0$, $O(\{\bar{n}_{\mathrm{m_q}}\}) < 1$. Since $\eta^2_{\mathrm{m_1}} \ll 1$, the term $O(\{\bar{n}_{\mathrm{m_q}}\})$ is closer to unity when $\bar{n}$ is small, while it is increasingly far from one as $\bar{n}$ increases. Because of the definition of χ_c in (40), when $t > 0$, for the same value of $p_r = p$, the geometric phase becomes smaller in the presence of warmer phonons, i.e., $\chi_c(\bar{n} > 0) < \chi_c(\bar{n} = 0)$. All terms with cos will then be closer to one for $\chi_c(\bar{n} > 0)$ values, and consequently, the success probability gets higher in the presence of warm phonons $P_r(\chi_c(\bar{n} > 0)) > P_r(\chi_c(\bar{n} = 0))$. This behavior can be observed in the bottom panel of Fig. 6, where the contour plot shows that the average success probability increases with $\bar{n}$. Regarding the average gate fidelity, in the presence of warm phonons, this can be written as

$$\bar{\mathcal{F}}^{\mathrm{f}}_g = \frac{1}{5}\left(1 + \frac{|\cos^2(\chi_c) + 2\cos(\chi_c)\sqrt{\bar{p}} + \bar{p}^2|^2}{4P_r}\right) \quad (44)$$

Similarly to the success probability in (43), the numerator in the second term of the right-hand side of Eq. (44) will become greater with increasing values of $\bar{n}$ since $\chi_c(\bar{n} > 0) < \chi_c(\bar{n} = 0)$. However, since the factor P_r in the denominator also increases with $\bar{n}$, the effect of warm phonons on the average gate fidelity is not as clear as in the success probability case. The behavior of both, fidelity and success probability in the presence of warm phonons is summarized in the top and bottom panel of Fig. 6, respectively. The top panel presents a contour plot for the simulated filtered gate fidelity $\bar{\mathcal{F}}^{\mathrm{f}}_g$ as a function of the amplitude decay time T_1 and the average number of phonons $\bar{n}$, where we considered the four modes to have the same occupation phonon number $\bar{n} = n_{\mathrm{m_1}} = n_{\mathrm{m_2}} = n_{\mathrm{m_3}} = n_{\mathrm{m_4}}$. We see that for times $t/T_1 < 1/2$, the effect of higher phonon numbers $\bar{n}$ barely affects the filtered gate fidelity; all contour plot lines appear nearly vertical. In this situation, the reversal operations following the implementation of scheme B are quite robust against thermal motion. On the other hand, for longer decay times $t \rightarrow T_1$, the filtered fidelity worsens slightly as one increases the average phonon number $\bar{n}$. Nevertheless, this scheme is considerably more robust than scheme A. It is also noteworthy to discuss the effect of increasing $\bar{n}$ on the success probability P_r in the bottom panel of Fig. 6. In this case, the chance of a correct reversal increases with larger values $\bar{n}$. The effect is most significant for larger t/T_1 but is still appreciable for shorter times ($t/T_1 < 1/2$). We conclude that the presence of warm active and spectator phonons on the trap axis direction could limit the distillation capabilities of scheme B when $t \rightarrow T_1$, but it has almost no effect at shorter times ($t/T_1 < 1/2$), even for $\bar{n} > 50$. It is also interesting to note that in the case considered here with $\eta_1 = 0.026$, the error contribution due to thermal modes in Eq. (41) is smaller than that resulting from larger values of the Lamb-Dicke parameter [109]. However, even in the presence of larger Lamb-Dicke parameters, the impact on the performance of scheme B would not be qualitatively much different. It would mainly be noticeable in the y-axis scale of Fig. 6, where the average phonon number $\bar{n}$ would take lower values.

In the presence of warm phonons, for a small probability of amplitude decay p, corresponding to large T_1, Eq. (1), the average gate fidelity is affected to a lesser extent than the success fidelity (compare the leftmost side of both panels in Fig. 6). This means that for small p, it is possible that working with a finite temperature of phonons in the ion chain becomes advantageous for scheme B, by increasing the chances of applying the filtering protocol successfully with little effect on the average gate fidelity.

V. CONCLUSIONS AND OUTLOOK

We have presented a method to perform probabilistic suppression of amplitude damping to protect any maximally entangled pair of trapped ion qubits from spontaneous photon scattering taking place during or after two-qubit entangling gates. The proposed method can be understood as a nonunitary filter that allows for single-copy quasidistillation. It can be applied to situations where the physical qubits are distant and where performing the conventional stabilizer readout of encoded quantum states is not straightforward. We have shown that such a filter can be obtained by postselecting on a weak measurement implemented via ancillary ions. The filter can be realized by either a QLS-based scheme or an entangling-gate scheme. In both cases, the nonunitary filter helps to reduce the overhead in the number of physical and ancillary qubits that is typically found in even the smallest QEC codes [40,41]. It can therefore be visualized as an alternative protection method that complements other error suppression approaches such as dynamical decoupling or encoding into decoherence-free subspaces. The method is clearly useful for platforms that focus on a small number of trapped ions such as clocks, sensors or quantum repeaters. We have also analyzed the role of thermal fluctuations on the amplitude damping reversal, which generate a possible source of noise. We showed that such fluctuations can constitute a limiting factor in the QLS scheme, while the entangling gate scheme is not only less sensitive to thermal fluctuations but may benefit from these at longer operation times. Other possible limitations to long storage times of trapped ions may stem from decay of the auxiliary metastable excited $|r\rangle$ state in the lambda configuration used in scheme A for the realization of the quantum measurement reversal POVM, and from the choice of ancilla qubits. These issues can be overcome by choosing $|r\rangle$ states with larger relaxation times and using ancillas from a different isotope or atomic species. Another limitation may be imposed by the heating rate of the vibrational modes, especially for the QLS-based method that requires the qubits to remain in the ground-state of motion throughout the protocol. Future studies directed towards laboratory implementation of the protocol should consider these additional error sources, as well as the effects of control imperfections in the various pulses. Another interesting application of the present amplitude damping reversal achieved by the nonunitary filter could be the detection of qubit leakage.

ACKNOWLEDGMENTS

A.R.B. acknowledges support by the Universidad Complutense de Madrid-Banco Santander Predoctoral Fellowship, the Fulbright Predoctoral Scholarship program (Fulbright Spain 2019-2020), and by GRADIANT, ICT R&D center in Galicia. A.R.B. also thanks J.G.F.U. for providing access to computing capabilities to carry out the numerical simulations. A.B. acknowledges support from PID2021-127726NB-I00 (MCIU/AEI/FEDER, UE), from the Grant IFT Centro de Excelencia Severo Ochoa CEX2020-001007-S, funded by MCIN/AEI/10.13039/501100011033, from the grant QUITEMAD+ S2013/ICE-2801, and from the CSIC Research Platform on Quantum Technologies PTI-001. K.B.W. was supported by the NSF QLCI program through grant number QMA-2016345.

---

[1] C. H. Bennett, G. Brassard, C. Crépeau, R. Jozsa, A. Peres, and W. K. Wootters, Phys. Rev. Lett. **70**, 1895 (1993).

[2] M. A. Nielsen and I. L. Chuang, *Quantum Computation and Quantum Information* (Cambridge University Press, Cambridge, 2000).

[3] N. Gisin and R. Thew, Nat. Photonics **1**, 165 (2007).

[4] B. Casabone, A. Stute, K. Friebe, B. Brandstätter, K. Schüppert, R. Blatt, and T. E. Northup, Phys. Rev. Lett. **111**, 100505 (2013).

[5] D. Lago-Rivera, S. Grandi, J. V. Rakonjac, A. Seri, and H. de Riedmatten, Nature (London) **594**, 37 (2021).

[6] C. J. Ballance, L. J. Stephenson, D. P. Nadlinger, B. C. Nichol, S. An, J. F. Goodwin, P. Drmota, and D. M. Lucas, in *Quantum Information and Measurement (QIM) V: Quantum Technologies* (Optica Publishing Group, Rome, 2019), p. S2D.1.

[7] S. Zaiser, T. Rendler, I. Jakobi, T. Wolf, S.-Y. Lee, S. Wagner, V. Bergholm, T. Schulte-Herbrüggen, P. Neumann, and J. Wrachtrup, Nat. Commun. **7**, 12279 (2016).

[8] C. L. Degen, F. Reinhard, and P. Cappellaro, Rev. Mod. Phys. **89**, 035002 (2017).

[9] M. Pfender, N. Aslam, H. Sumiya, S. Onoda, P. Neumann, J. Isoya, C. A. Meriles, and J. Wrachtrup, Nat. Commun. **8**, 834 (2017).

[10] J. Preskill, Proc. R. Soc. London, Ser. A **454**, 385 (1998).

[11] T. D. Ladd, F. Jelezko, R. Laflamme, Y. Nakamura, C. Monroe, and J. L. O'Brien, Nature (London) **464**, 45 (2010).

[12] P. W. Shor, Phys. Rev. A **52**, R2493 (1995).

[13] P. Staanum, I. S. Jensen, R. G. Martinussen, D. Voigt, and M. Drewsen, Phys. Rev. A **69**, 032503 (2004).

[14] D. Nigg, J. T. Barreiro, P. Schindler, M. Mohseni, T. Monz, M. Chwalla, M. Hennrich, and R. Blatt, Phys. Rev. Lett. **110**, 060403 (2013).

[15] P. Schindler, D. Nigg, T. Monz, J. T. Barreiro, E. Martinez, S. X. Wang, S. Quint, M. F. Brandl, V. Nebendahl, C. F. Roos, M. Chwalla, M. Hennrich, and R. Blatt, New J. Phys. **15**, 123012 (2013).

[16] C. R. Clark, H. N. Tinkey, B. C. Sawyer, A. M. Meier, K. A. Burkhardt, C. M. Seck, C. M. Shappert, N. D. Guise, C. E. Volin, S. D. Fallek, H. T. Hayden, W. G. Rellergert, and K. R. Brown, Phys. Rev. Lett. **127**, 130505 (2021).

[17] J. P. Gaebler, T. R. Tan, Y. Lin, Y. Wan, R. Bowler, A. C. Keith, S. Glancy, K. Coakley, E. Knill, D. Leibfried, and D. J. Wineland, Phys. Rev. Lett. **117**, 060505 (2016).

[18] C. J. Ballance, T. P. Harty, N. M. Linke, M. A. Sepiol, and D. M. Lucas, Phys. Rev. Lett. **117**, 060504 (2016).

[19] D. J. Wineland, C. Monroe, W. M. Itano, D. Leibfried *et al.*, J. Res. Natl. Inst. Stand. Technol. **103**, 259 (1998).

[20] R. Ozeri, W. M. Itano, R. B. Blakestad, J. Britton, J. Chiaverini, J. D. Jost, C. Langer, D. Leibfried, R. Reichle, S. Seidelin, J. H. Wesenberg, and D. J. Wineland, Phys. Rev. A **75**, 042329 (2007).

[21] S. de Léséleuc, D. Barredo, V. Lienhard, A. Browaeys, and T. Lahaye, Phys. Rev. A **97**, 053803 (2018).

[22] M. Saffman, I. I. Beterov, A. Dalal, E. J. Páez, and B. C. Sanders, Phys. Rev. A **101**, 062309 (2020).

[23] D. Bluvstein, H. Levine, G. Semeghini, T. T. Wang, S. Ebadi, M. Kalinowski, A. Keesling, N. Maskara, H. Pichler, M. Greiner, V. Vuletić, and M. D. Lukin, Nature (London) **604**, 451 (2022).

[24] D. Gottesman, arXiv:0904.2557.

[25] *Quantum Error Correction*, edited by D. Lidar and T. Brun (Cambridge University Press, Cambridge, 2013).

[26] J. Roffe, Contemp. Phys. **60**, 226 (2019).

[27] D. Nigg, M. Müller, E. A. Martinez, P. Schindler, M. Hennrich, T. Monz, M. A. Martin-Delgado, and R. Blatt, Science **345**, 302 (2014).

[28] C. Ryan-Anderson, J. G. Bohnet, K. Lee, D. Gresh, A. Hankin, J. P. Gaebler, D. Francois, A. Chernoguzov, D. Lucchetti, N. C. Brown, T. M. Gatterman, S. K. Halit, K. Gilmore, J. A. Gerber, B. Neyenhuis, D. Hayes, and R. P. Stutz, Phys. Rev. X **11**, 041058 (2021).

[29] L. Postler, S. Heußen, I. Pogorelov, M. Rispler, T. Feldker, M. Meth, C. D. Marciniak, R. Stricker, M. Ringbauer, R. Blatt, P. Schindler, M. Müller, and T. Monz, Nature (London) **605**, 675 (2022).

[30] Y. Zhao, Y. Ye, H.-L. Huang, Y. Zhang, D. Wu, H. Guan, Q. Zhu, Z. Wei, T. He, S. Cao, F. Chen, T.-H. Chung, H. Deng, D. Fan, M. Gong, C. Guo, S. Guo, L. Han, N. Li, S. Li, Y. Li, F. Liang, J. Lin, H. Qian, H. Rong, H. Su, L. Sun, S. Wang, Y. Wu, Y. Xu, C. Ying, J. Yu, C. Zha, K. Zhang, Y.-H. Huo, C.-Y. Lu, C.-Z. Peng, X. Zhu, and J.-W. Pan, Phys. Rev. Lett. **129**, 030501 (2022).

[31] S. Krinner, N. Lacroix, A. Remm, A. Di Paolo, E. Genois, C. Leroux, C. Hellings, S. Lazar, F. Swiadek, J. Herrmann, G. J. Norris, C. K. Andersen, M. Müller, A. Blais, C. Eichler, and A. Wallraff, Nature (London) **605**, 669 (2022).

[32] R. Acharya, I. Aleiner, R. Allen, T. I. Andersen, M. Ansmann, F. Arute, K. Arya, A. Asfaw, J. Atalaya, R. Babbush, D. Bacon, J. C. Bardin, J. Basso, A. Bengtsson, S. Boixo, G. Bortoli, A. Bourassa, J. Bovaird, L. Brill *et al.*, arXiv:2207.06431.

[33] C. Ryan-Anderson, N. C. Brown, M. S. Allman, B. Arkin, G. Asa-Attuah, C. Baldwin, J. Berg, J. G. Bohnet, S. Braxton, N. Burdick, J. P. Campora, A. Chernoguzov, J. Esposito, B. Evans, D. Francois, J. P. Gaebler, T. M. Gatterman, J. Gerber, K. Gilmore, D. Gresh, A. Hall, A. Hankin, J. Hostetter, D. Lucchetti, K. Mayer, J. Myers, B. Neyenhuis, J. Santiago, J. Sedlacek, T. Skripka, A. Slattery, R. P. Stutz, J. Tait, R. Tobey, G. Vittorini, J. Walker, and D. Hayes, arXiv:2208.01863.

[34] D. Aharonov and M. Ben-Or, SIAM J. Comput. **38**, 1207 (2008).

[35] B. M. Terhal, Rev. Mod. Phys. **87**, 307 (2015).

[36] E. Knill, R. Laflamme, and W. H. Zurek, Proc. R. Soc. London, Ser. A **454**, 365 (1998).

[37] D. Gottesman, arXiv:quant-ph/0507174.

[38] L. Viola and S. Lloyd, Phys. Rev. A **58**, 2733 (1998).

[39] D. A. Lidar, I. L. Chuang, and K. B. Whaley, Phys. Rev. Lett. **81**, 2594 (1998).

[40] D. W. Leung, M. A. Nielsen, I. L. Chuang, and Y. Yamamoto, Phys. Rev. A **56**, 2567 (1997).

[41] A. S. Fletcher, P. W. Shor, and M. Z. Win, IEEE Trans. Inf. Theory **54**, 5705 (2008).

[42] W. Dür and H. J. Briegel, Rep. Prog. Phys. **70**, 1381 (2007).

[43] C. H. Bennett, G. Brassard, S. Popescu, B. Schumacher, J. A. Smolin, and W. K. Wootters, Phys. Rev. Lett. **76**, 722 (1996).

[44] H.-J. Briegel, W. Dür, J. I. Cirac, and P. Zoller, Phys. Rev. Lett. **81**, 5932 (1998).

[45] M. B. Plenio and S. Virmani, Quantum Info. Comput. **7**, 1 (2007).

[46] L. Aolita, F. de Melo, and L. Davidovich, Rep. Prog. Phys. **78**, 042001 (2015).

[47] M. Horodecki, P. Horodecki, and R. Horodecki, Phys. Rev. Lett. **78**, 574 (1997).

[48] C. H. Bennett, H. J. Bernstein, S. Popescu, and B. Schumacher, Phys. Rev. A **53**, 2046 (1996).

[49] N. Gisin, Phys. Lett. A **210**, 151 (1996).

[50] P. G. Kwiat, S. Barraza-Lopez, A. Stefanov, and N. Gisin, Nature (London) **409**, 1014 (2001).

[51] M. A. Nielsen, Phys. Lett. A **303**, 249 (2002).

[52] M. Koashi and M. Ueda, Phys. Rev. Lett. **82**, 2598 (1999).

[53] M. Ueda and M. Kitagawa, Phys. Rev. Lett. **68**, 3424 (1992).

[54] J.-W. Pan, S. Gasparoni, R. Ursin, G. Weihs, and A. Zeilinger, Nature (London) **423**, 417 (2003).

[55] T. Yamamoto, M. Koashi, Ş. K. Özdemir, and N. Imoto, Nature (London) **421**, 343 (2003).

[56] Z. Zhao, T. Yang, Y.-A. Chen, A.-N. Zhang, and J.-W. Pan, Phys. Rev. Lett. **90**, 207901 (2003).

[57] R. Reichle, D. Leibfried, E. Knill, J. Britton, R. B. Blakestad, J. D. Jost, C. Langer, R. Ozeri, S. Seidelin, and D. J. Wineland, Nature (London) **443**, 838 (2006).

[58] J. A. Sherman, M. J. Curtis, D. J. Szwer, D. T. C. Allcock, G. Imreh, D. M. Lucas, and A. M. Steane, Phys. Rev. Lett. **111**, 180501 (2013).

[59] A. Kent, Phys. Rev. Lett. **81**, 2839 (1998).

[60] N. Linden, S. Massar, and S. Popescu, Phys. Rev. Lett. **81**, 3279 (1998).

[61] M. Horodecki, P. Horodecki, and R. Horodecki, Phys. Rev. A **60**, 1888 (1999).

[62] F. Verstraete, J. Dehaene, and B. DeMoor, Phys. Rev. A **64**, 010101(R) (2001).

[63] Y. Ota, S. Ashhab, and F. Nori, J. Phys. A: Math. Theor. **45**, 415303 (2012).

[64] Z. Liao, M. Al-Amri, and M. S. Zubairy, J. Phys. B: At., Mol. Opt. Phys. **46**, 145501 (2013).

[65] A. N. Korotkov and A. N. Jordan, Phys. Rev. Lett. **97**, 166805 (2006).

[66] Q. Sun, M. Al-Amri, L. Davidovich, and M. S. Zubairy, Phys. Rev. A **82**, 052323 (2010).

[67] J. Preskill, *Lecture Notes for Physics 219: Quantum Computation* (California Institute of Technology, Pasadena, 1998).

[68] P. O. Schmidt, T. Rosenband, C. Langer, W. M. Itano, J. C. Bergquist, and D. J. Wineland, Science **309**, 749 (2005).

[69] J. P. Home, in *Advances in Atomic, Molecular, and Optical Physics*, edited by E. Arimondo, P. R. Berman, and C. C. Lin (Academic Press, 2013), Vol. 62, pp. 231–277.

[70] C. D. Bruzewicz, R. McConnell, J. Stuart, J. M. Sage, and J. Chiaverini, npj Quantum Inf. **5**, 102 (2019).

[71] P. Dhara, N. M. Linke, E. Waks, S. Guha, and K. P. Seshadreesan, Phys. Rev. A **105**, 022623 (2022).

[72] D. L. Moehring, P. Maunz, S. Olmschenk, K. C. Younge, D. N. Matsukevich, L.-M. Duan, and C. Monroe, Nature (London) **449**, 68 (2007).

[73] D. N. Matsukevich, P. Maunz, D. L. Moehring, S. Olmschenk, and C. Monroe, Phys. Rev. Lett. **100**, 150404 (2008).

[74] S. Pironio, A. Acín, S. Massar, A. B. de la Giroday, D. N. Matsukevich, P. Maunz, S. Olmschenk, D. Hayes, L. Luo, T. A. Manning, and C. Monroe, Nature (London) **464**, 1021 (2010).

[75] D. Hucul, I. V. Inlek, G. Vittorini, C. Crocker, S. Debnath, S. M. Clark, and C. Monroe, Nat. Phys. **11**, 37 (2015).

[76] L. J. Stephenson, D. P. Nadlinger, B. C. Nichol, S. An, P. Drmota, T. G. Ballance, K. Thirumalai, J. F. Goodwin, D. M. Lucas, and C. J. Ballance, Phys. Rev. Lett. **124**, 110501 (2020).

[77] D. P. Nadlinger, P. Drmota, B. C. Nichol, G. Araneda, D. Main, R. Srinivas, D. M. Lucas, C. J. Ballance, K. Ivanov, E. Y.-Z. Tan, P. Sekatski, R. L. Urbanke, R. Renner, N. Sangouard, and J.-D. Bancal, Nature (London) **607**, 682 (2022).

[78] B. C. Nichol, R. Srinivas, D. P. Nadlinger, P. Drmota, D. Main, G. Araneda, C. J. Ballance, and D. M. Lucas, arXiv:2111.10336.

[79] A. G. Kofman, S. Ashhab, and F. Nori, Phys. Rep. **520**, 43 (2012).

[80] Y.-S. Kim, Y.-W. Cho, Y.-S. Ra, and Y.-H. Kim, Opt. Express **17**, 11978 (2009).

[81] N. Katz, M. Ansmann, R. C. Bialczak, E. Lucero, R. McDermott, M. Neeley, M. Steffen, E. M. Weig, A. N. Cleland, J. M. Martinis, and A. N. Korotkov, Science **312**, 1498 (2006).

[82] N. Katz, M. Neeley, M. Ansmann, R. C. Bialczak, M. Hofheinz, E. Lucero, A. O'Connell, H. Wang, A. N. Cleland, J. M. Martinis, and A. N. Korotkov, Phys. Rev. Lett. **101**, 200401 (2008).

[83] Y. P. Zhong, Z. L. Wang, J. M. Martinis, A. N. Cleland, A. N. Korotkov, and H. Wang, Nat. Commun. **5**, 3135 (2014).

[84] S. K. Choudhary, T. Konrad, and H. Uys, Phys. Rev. A **87**, 012131 (2013).

[85] Y.-S. Kim, J.-C. Lee, O. Kwon, and Y.-H. Kim, Nat. Phys. **8**, 117 (2012).

[86] J.-C. Lee, Y.-C. Jeong, Y.-S. Kim, and Y.-H. Kim, Opt. Express **19**, 16309 (2011).

[87] M. Siomau and A. A. Kamli, Phys. Rev. A **86**, 032304 (2012).
[88] Z.-X. Man, Y.-J. Xia, and N. B. An, Phys. Rev. A **86**, 012325 (2012).
[89] X.-W. Wang, S. Yu, D.-Y. Zhang, and C. H. Oh, Sci. Rep. **6**, 22408 (2016).
[90] D. Leibfried, B. DeMarco, V. Meyer, D. Lucas, M. Barrett, J. Britton, W. M. Itano, B. Jelenković, C. Langer, T. Rosenband, and D. J. Wineland, Nature (London) **422**, 412 (2003).
[91] D. Kielpinski, C. Monroe, and D. J. Wineland, Nature (London) **417**, 709 (2002).
[92] V. Kaushal, B. Lekitsch, A. Stahl, J. Hilder, D. Pijn, C. Schmiegelow, A. Bermudez, M. Müller, F. Schmidt-Kaler, and U. Poschinger, AVS Quantum Sci. **2**, 014101 (2020).
[93] W. C. Campbell, Phys. Rev. A **102**, 022426 (2020).
[94] K. Mølmer and A. Sørensen, Phys. Rev. Lett. **82**, 1835 (1999).
[95] A. Sørensen and K. Mølmer, Phys. Rev. Lett. **82**, 1971 (1999).
[96] R. Ozeri, Contemp. Phys. **52**, 531 (2011).
[97] B. Schumacher, Phys. Rev. A **54**, 2614 (1996).
[98] N. Johnston and D. W. Kribs, J. Phys. A: Math. Theor. **44**, 495303 (2011).
[99] B. M. Terhal, Phys. Lett. A **271**, 319 (2000).
[100] R. Horodecki, P. Horodecki, M. Horodecki, and K. Horodecki, Rev. Mod. Phys. **81**, 865 (2009).
[101] G. Tóth and O. Gühne, Phys. Rev. A **72**, 022340 (2005).
[102] A. Rodriguez-Blanco, A. Bermudez, M. Müller, and F. Shahandeh, PRX Quantum **2**, 020304 (2021).
[103] J. Hilder, D. Pijn, O. Onishchenko, A. Stahl, M. Orth, B. Lekitsch, A. Rodriguez-Blanco, M. Müller, F. Schmidt-Kaler, and U. G. Poschinger, Phys. Rev. X **12**, 011032 (2022).
[104] G. Milburn, S. Schneider, and D. James, Fortschr. Phys. **48**, 801 (2000).
[105] A. Sørensen and K. Mølmer, Phys. Rev. A **62**, 022311 (2000).
[106] A. Bermudez, X. Xu, R. Nigmatullin, J. O'Gorman, V. Negnevitsky, P. Schindler, T. Monz, U. G. Poschinger, C. Hempel, J. Home, F. Schmidt-Kaler, M. Biercuk, R. Blatt, S. Benjamin, and M. Müller, Phys. Rev. X **7**, 041061 (2017).
[107] A. Bermudez, T. Schaetz, and M. B. Plenio, Phys. Rev. Lett. **110**, 110502 (2013).
[108] D. F. V. James, Appl. Phys. B: Lasers Opt. **66**, 181 (1998).
[109] D. Kienzler, H.-Y. Lo, V. Negnevitsky, C. Flühmann, M. Marinelli, and J. P. Home, Phys. Rev. Lett. **119**, 033602 (2017).